The Mean Kinematic Structure of the Tropical Cyclone Boundary Layer and Its Relationship to Intensity Change

Jun A. Zhang[a,b] Robert F. Rogers,[a] Paul D. Reasor,[a] and John Gamache[a]

[a] *NOAA/AOML/Hurricane Research Division, Miami, Florida*
[b] *University of Miami/CIMAS, Miami, Florida*

ABSTRACT: This study investigates the relationship between the azimuthally averaged kinematic structure of the tropical cyclone boundary layer (TCBL) and storm intensity, intensity change, and vortex structure above the BL. These relationships are explored using composites of airborne Doppler radar vertical profiles, which have a higher vertical resolution than typically used three-dimensional analyses and, therefore, better capture TCBL structure. Results show that the BL height, defined by the depth of the inflow layer, is greater in weak storms than in strong storms. The inflow layer outside the radius of maximum tangential wind speed (RMW) is deeper in intensifying storms than in nonintensifying storms at an early stage. The peak BL convergence inside the RMW is larger in intensifying storms than in nonintensifying storms. Updrafts originating from the TCBL are concentrated near the RMW for intensifying TCs, while updrafts span a large radial range outside the RMW for nonintensifying TCs. In terms of vortex structure above the BL, storms with a quickly decaying radial profile of tangential wind outside the RMW ("narrow" vortices) tend to have a deeper inflow layer outside the RMW, stronger inflow near the RMW, deeper and more concentrated strong updrafts close to the RMW, and weaker inflow in the outer core region than those with a slowly decaying tangential wind profile ("broad" vortices). The narrow TCs also tend to intensify faster than broad TCs, suggesting that a key relationship exists among vortex shape, the BL kinematic structure, and TC intensity change. This relationship is further explored by comparisons of absolute angular momentum budget terms for each vortex shape.

KEYWORDS: Boundary layer; Tropical cyclones; Air-sea interaction; Budgets; Aircraft observations; Radars/Radar observations

1. Introduction

A major challenge in tropical cyclone (TC) research and forecasting is to understand and predict the physical processes underlying TC intensity change (Gall et al. 2013; Cangialosi et al. 2020). The difficulty for intensity forecasting is partly due to a lack of understanding of the physical processes governing TC intensity change (Kaplan et al. 2015) that span multiple spatial and temporal scales. Early theories of TC intensification took an essentially axisymmetric view of the vortex evolution and underlying physical processes (e.g., Ooyama 1969; Emanuel 1986, 1995). Studies employing an axisymmetric balance framework (i.e., vortex constrained to evolve in gradient and hydrostatic balance) in particular have focused on the radial location of diabatic heating and the symmetric vortex response to this heating (Schubert and Hack 1982; Shapiro and Willoughby 1982; Hack and Schubert 1986; Nolan et al. 2007; Pendergrass and Willoughby 2009; Vigh and Schubert 2009; Heng and Wang 2016). Observational studies, including airborne Doppler radar data (Rogers et al. 2013) and flight-level and satellite-derived lightning data (Stevenson et al. 2018), have documented a relationship where deep convection preferentially located inside the radius of maximum wind (RMW) was associated with intensifying TCs, while deep convection preferentially located radially outward, at the RMW or outside, was associated with

nonintensifying TCs. One interpretation of these observations within the axisymmetric balance framework is that the efficiency of diabatic heating from deep convection is enhanced when the heating occurs within the high inertial stability region inside the RMW (e.g., Hack and Schubert 1986; Nolan et al. 2007; Pendergrass and Willoughby 2009).

Smith and Montgomery (2016) offered an alternate, and arguably more direct, explanation for the dependence of intensification rate on the radial location of heating by noting that the lower branch of the heating-induced secondary circulation will tend to advect angular momentum surfaces inward (outward) across the RMW and strengthen (weaken) the maximum wind when the heating is positioned inside (outside) of the RMW. This explanation is tied to the conventional balance spinup mechanism (Ooyama 1969). They cautioned, however, that understanding intensification cannot be accomplished apart from explicit consideration of the dynamics and thermodynamics of the TC boundary layer (BL). Essentially, in terms of the dynamics, agradient forcing in the boundary layer helps spin up a TC vortex when the inflowing air radially advects absolute angular momentum at a rate exceeding the rate of removal by the frictional torque, referred to by Montgomery and Smith (2014) as the boundary layer spinup mechanism. Montgomery et al. (2014a) and Sanger et al. (2014) have illustrated this mechanism using case studies with dropsonde data. The coupling between the flow within the TCBL and the flow above, and the coupling between the boundary layer and conventional spinup mechanisms, means that generally it is not possible to isolate any

one process as causing TC intensification (Montgomery and Smith 2014; Kilroy et al. 2016; Smith et al. 2021).

In a recent study of the TC life cycle in an idealized, quiescent environment, Smith et al. (2021) examined this coupling during periods of intensification, steady state intensity and weakening. A period of transient (~1–2 days) weakening in particular illustrated the complex relationship between eyewall vertical mass flux, flow changes above the boundary layer, TCBL processes, and rainband development. One of the key findings near the onset of the weakening period is a reduction in the ability of eyewall convection to ventilate air exiting the TCBL within the eyewall. Although the vertical mass flux above the TCBL can be approximated reasonably by the balanced response to diabatic heating in the eyewall region, the heating magnitude itself depends on the thermodynamic structure of the TCBL. Furthermore, according to the boundary layer control mechanism articulated by Kilroy et al. (2016), outside the immediate vicinity of the eyewall updraft, the radial inflow and vertical motion within the TCBL are largely determined by the TCBL dynamics. The spatial distribution of heating (e.g., RMW-relative location of peak heating) is then tied to the radial convergence governed by the TCBL dynamics. With the eyewall convection unable to ventilate all of the air exiting the TCBL, radially extensive outflow develops at its top which 1) causes angular momentum surfaces to move outward, promoting local vortex spindown above the TCBL and 2) was argued to support rainband development well outside the eyewall (Kilroy et al. 2016; Smith et al. 2021). The transient weakening of the peak wind in the TCBL proceeds as the reduced (gradient balanced) pressure gradient field is communicated to the TCBL, and, through the TCBL dynamics, inflow and angular momentum advection near the eyewall are reduced. At the same time, the greater rainband activity appears to disrupt the prior symmetry and vigor of eyewall convection. This, too, is likely to have a negative impact on intensification through the decreased convective mass flux available to ventilate the air flowing out of the TCBL and the attendant enhancement of low-level radial outflow (Smith et al. 2021). While the discussion above has focused on the weakening stage of TCs, similar reasoning can be applied for the intensification stage, except in that case the convective mass flux is able to ventilate the air flowing out of the TCBL, and in fact can result in a net inward mass flux above the TCBL that advects higher angular momentum air inward (i.e., the conventional spinup mechanism).

As noted above, it is impossible to point to any one of these mechanisms as causing TC intensification or weakening owing to the substantial coupling between them. We take a similar view here in our analysis of radar-observed TCBL structure and its relationship to intensity change. That is, we examine what the TCBL kinematic structure conveys about its contribution to intensity change, but avoid cause and effect type arguments based on that structure. Rather, the objectives here are to exploit the capabilities of Doppler radar vertical profile data to document the azimuthal-mean kinematic structure with horizontal scales > 1.5 km and vertical scales > 150 m and characterize how this structure varies as a function of vortex-scale structure and intensity change rate. Such an examination

can shed insight on the validity of the processes and relationships described above.

2. Data and methodology

a. Airborne Doppler profile analyses

In this study, vertical profile data from NOAA WP-3D tail Doppler radar (TDR) observations are analyzed. TDR data has helped improve our understanding of the multiscale structure of hurricanes (e.g., Marks 1985; Marks and Houze 1987; Gamache et al. 1995; Marks et al. 1992, 2008; Reasor and Eastin 2012; Guimond et al. 2016a; Rogers et al. 2015, 2019; Fischer et al. 2022). The TDR on the WP-3D aircraft scans in cones 20° fore and aft of the plane normal to the length of the fuselage. The analysis of the three wind components can be done in three dimensions along the flight track of the radar, but this requires the solution of the mass continuity equation which tends to smooth the wind solution. The number of points in the aforementioned three-dimensional variational solution is limited by computer memory and execution-time constraints. Thus, the vertical spacing of the analysis in most cases is limited to 500 m. To avoid both the smoothing resulting from integrating the mass-continuity solution and the limited vertical resolution, a vertical profile analysis method was developed. Our purpose here is to clarify aspects of this method that was first described by Lorsolo et al. (2010) but may not have been evident in their presentation. We also update the description to the current configuration used in operations.

The vertical profile analysis method assumes that the radial, tangential (azimuthal), and vertical winds are constant within a grid cell that extends 1.5 km inward and outward from the grid point location along the flight track (i.e., 3 km wide in radius), 150 m above and below the grid point, and up to 10 km in arc (i.e., arc centered on storm center) on either side of the flight track (Fig. 1a). Grid points along the aircraft track are determined every 1.5 km in radius and 150 m in height. This affords a somewhat smoother appearance than if each grid cell had totally different observations. Only radials with Earth-relative elevations greater (lower) than 30° (−30°) are used, so that when the aircraft flies at ~3-km altitude, the Doppler radials used below the aircraft (most relevant to the present study) are within 6 km on either side of the aircraft near the surface, and within an increasingly narrower range from the surface up to the aircraft altitude. The choice of grid cell and its azimuthal dimension is designed to be as small as possible while affording enough angle diversity to determine all three wind components geometrically (Fig. 1b).

An advantage of using a grid cell based upon radius and azimuth, rather than along-track and cross-track dimension, is that the winds can be determined in a grid that does not change as the aircraft turns into the constantly changing crosswind and maneuvers around intense convective cells. The Doppler observations, recorded in an airframe-relative coordinate system, are converted to the Earth-relative coordinate system using the method of Lee et al. (1994). Since it is the radial and tangential winds that are determined, and not the
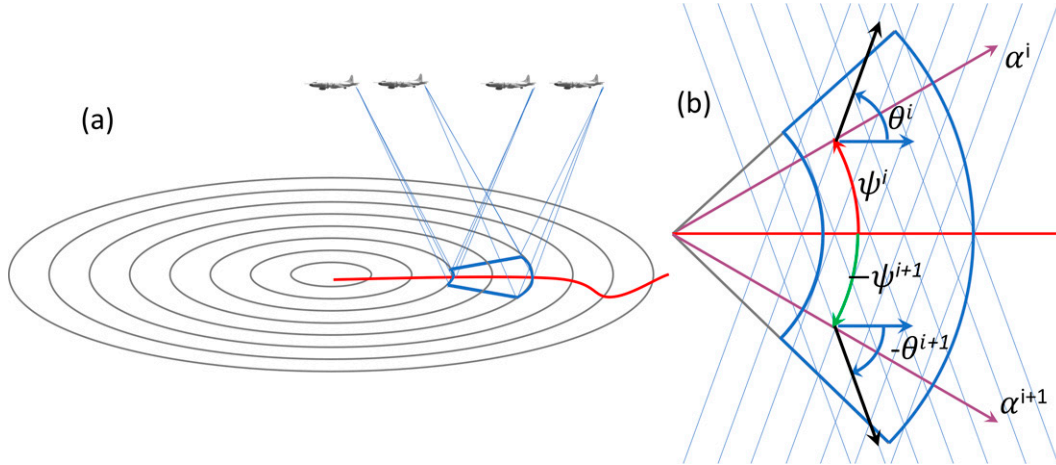
FIG. 1. (a) TDR scanning pattern (thin blue lines) at a given storm-relative grid cell (thick blue boundary) along the flight track (red line). (b) Plan view illustration of angles θ and ψ and direction cosine α (see text) associated with fore and aft Doppler measurements (cross-hatched thin blue lines) within a grid cell (thick blue boundary) centered on the flight track (red line). Black arrows indicate the horizontal projection of the Doppler observation vector for observations i and $i + 1$, and the base of the arrow indicates the actual location of the observation. Purple arrows indicate the direction along which direction cosines α^i and α^{i+1} are defined, and the directions of the direction cosines β^i and β^{i+1} (not shown) are perpendicular and to the left. Blue arrows indicate the due-east direction, θ is the angle between the horizontal projection of the Doppler-pointing direction and due east, defined counterclockwise from east, and ψ is the azimuth of the observation relative to the storm center defined counterclockwise from east. The grid cells are 3 km wide in radius, 300 m thick in height, and up to 10 km in azimuth (arc length).

Earth-relative Cartesian wind components, the direction cosines of the Doppler radials are computed based upon the azimuth at the location of the observation, relative to the storm center. The angular diversity of observations means that the radial (u), tangential (v), and vertical (W) precipitation motions in each grid cell are overdetermined and the solution minimizes the square of the difference between the projection of the precipitation motion and the Doppler radial velocity at each observation location, summed over all the equally weighted observations in the grid cell, as described by

$$J_O = \sum_{i=0}^{N} (V_{ro}^i - V_{rs}^i)^2, \tag{1}$$

where V_{ro}^i is the ith Doppler radial velocity observation within the grid cell, and

$$V_{rs}^i = \alpha^i u + \beta^i v + \gamma^i W. \tag{2}$$

The term V_{rs}^i is the projection of the overdetermined solution wind in the grid cell on the ith Doppler observation direction given by the direction cosines α^i (radial), β^i (azimuthal), and γ^i (vertical), which are defined by

$$\alpha^i = \cos\psi^i \cos\theta^i \cos\phi^i + \sin\psi^i \sin\theta^i \cos\phi^i, \tag{3}$$

$$\beta^i = -\sin\psi^i \cos\theta^i \cos\phi^i + \cos\psi^i \sin\theta^i \cos\phi^i, \tag{4}$$

$$\gamma^i = \sin\phi^i, \tag{5}$$

where θ is the angle between the horizontal projection of the Doppler pointing direction and due east, defined

counterclockwise, ϕ is the elevation angle defined positive upward, which is the angle between the Doppler radial and horizontal, and ψ is the azimuth of the observation relative to the storm center, defined counterclockwise from east. The J_0 may then be expressed as

$$J_0 = \sum_{i=0}^{N} (V_{ro}^i - \alpha^i u - \beta^i v - \gamma^i W)^2. \tag{6}$$

The J_0 is then minimized through least squares to give u, v, and W by solving the system of three equations:

$$\frac{\partial J_0}{\partial u} = 0, \ \frac{\partial J_0}{\partial v} = 0, \ \frac{\partial J_0}{\partial W} = 0. \tag{7}$$

Once the three components of precipitation motion are determined, then the estimated precipitation terminal fall speed V_T is subtracted from the vertical precipitation motion W to give the vertical wind w:

$$w = W - V_T, \tag{8}$$

where the fall speed in rain has the form of

$$V_T = -2.6 Z^{0.107} \left(\frac{\rho_0}{\rho}\right)^{0.45}, \tag{9}$$

while the fall speed in snow has the form of

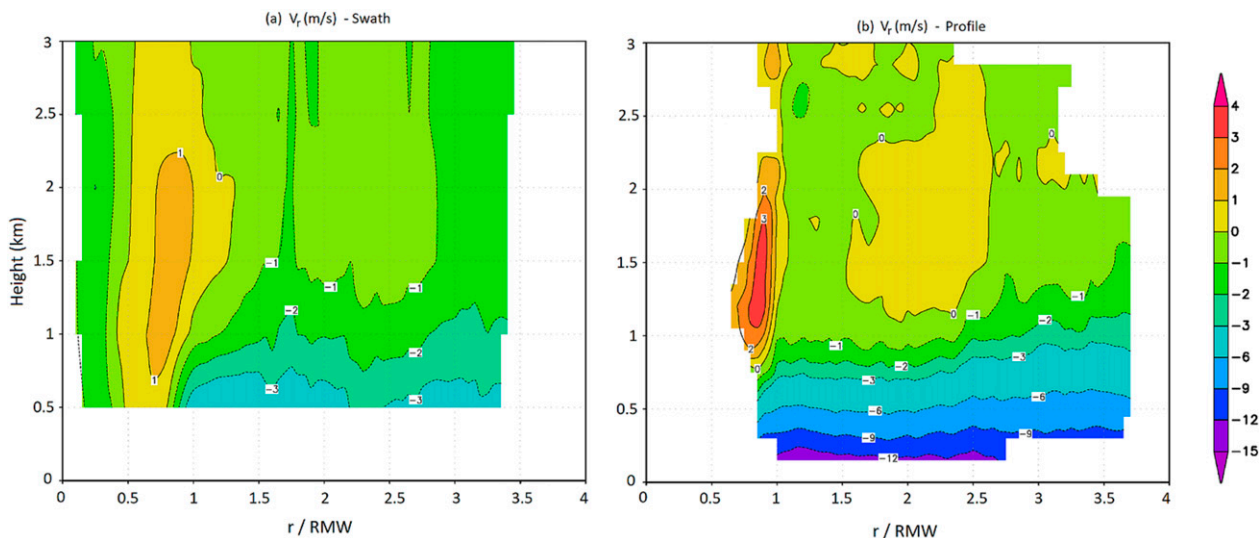$$V_T = -0.817 Z^{0.063} \left(\frac{\rho_0}{\rho}\right)^{0.45}. \tag{10}$$

FIG. 2. Composite axisymmetric radial wind (V_r) from (a) swath and (b) profile data. Data from a minimum of 20 analyses are required for plotting. Adapted from Figs. 7c and 7d of Rogers et al. (2012) using all radar legs in their Table 1.

Here, V_T is defined negative downward, Z is the averaged radar reflectivity within a grid cell, ρ is the air density at the grid point, and ρ_0 is the air density at sea level (Joss and Waldvogel 1970; Atlas et al. 1973). By first analyzing the vertical precipitation motion, it is possible to separate the snow above from the rain below in the stratiform regions, since there is an abrupt change in the diagnosed precipitation vertical motion at the melting level.

It is important to re-emphasize that the radial–vertical profile analysis described above is only truly a radial cross section through the TC to the extent that the flight track follows a constant azimuth. In reality, deviations from a nominal inbound or outbound azimuth are common and, thus, the vertical profile should always be interpreted in the context of the actual flight track. The vertical profile NetCDF files, which are currently produced during TC flight operations contain the radius and azimuth of each analysis grid point along the flight track, relative to the specified storm center.

Figure 2 shows a comparison of the swath and profile observations of radial winds from the composite analyses given by Rogers et al. (2012). The domain is zoomed into the lowest 3 km to highlight differences in the structure of the radial flow in the TCBL between the two different radar analyses. The peak inflow at 0.15-km altitude is consistent with composite dropsonde studies of TCBL structure (Bell and Montgomery 2008; Zhang et al. 2011; Ming et al. 2015; Ahern et al. 2019). The corner flow region, representing strong outflow inside the RMW above the top of the frictional inflow, is also more clearly observed by the profile data. This region is where the BL convergence occurs and where the radial location and strength of that convergence are determined. The vertical velocity measurements from the profile analysis are comparable to the swath analysis, though, as swath and profile analysis retrievals are subject to an RMS error of 1.6 and 1.4 m s^{-1}, respectively (see Table 2 of Rogers et al. 2012), when compared with flight-level measurements.

b. Cases used in the composite analysis

Table 1 summarizes the list of storms and number of flights used in this study. Frequency distributions of the best track storm intensity (V_{max}), 12-h intensity change from the time of the TDR observation, and RMW are presented in Fig. 3. The storm intensities range from 30 to 160 kt (1 kt ≈ 0.51 m s^{-1}), the intensity-change rates range from −60 to 30 kt (12 h)$^{-1}$, and the RMWs range from 15 to 160 km.

We use a composite analysis approach to analyze the profile data following Zhang et al. (2011) and Rogers et al. (2012), in which data are averaged as a function of the radius r that is normalized by the RMW at 600-m altitude; that is, $r^* = r/RMW_{600m}$, with a bin width of 0.1r^*. The horizontal views of the radial legs of the radar profile data in both Earth-relative and shear-relative frameworks are shown in Fig. 4, suggesting a reasonably good azimuthal coverage that is not biased toward a geographic or

TABLE 1. List of years, storm names, and numbers of P3 flights (in parentheses) for the Doppler profile data used in this study.

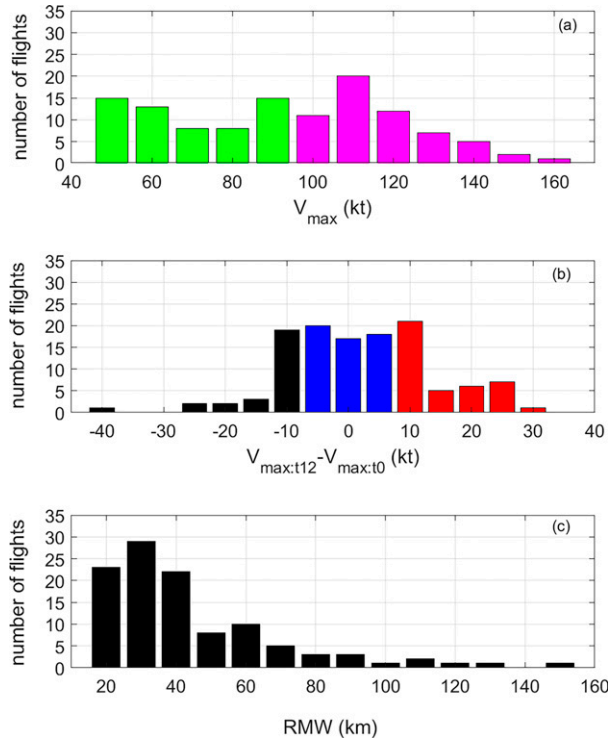| Year	Storm name (No. of flights)
1997	Guillermo (2)
2003	Fabian (3), Isabel (3)
2004	Frances (6), Ivan (10), Jeanne (5)
2005	Katrina (4), Ophelia (6), Rita (4), Wilma (1)
2007	Felix (2)
2008	Dolly (4), Fay (5), Gustav (5), Ike (1), Paloma (3)
2009	Bill (2)
2010	Earl (10)
2014	Arthur (2), Bertha (1), Cristobal (3), Edouard (6), Gonzalo (2)
2015	Danny (2)
2016	Earl (3), Karl (2), Matthew (5)
2019	Barry (5), Dorian (19), Humberto (4), Jerry (3), Lorenzo (3), Nestor (2)

FIG. 3. Histograms of (a) storm intensity (V_{max}; kt), (b) 12-h intensity change (V_{max}:t12 − V_{max}:t0; kt), and (c) radius of the maximum wind speed at 600-m altitude (RMW; km) associated with the Doppler profile data. The green color in (a) represents the weak TC group, while the pink color represents the strong TC group. The black color in (b) represents the weakening (WE) group, the blue color represents the steady-state (SS) group, and the red color represents the intensifying (INT) group.

shear-relative location within the TC. There are slightly (~4%) more radial legs on the downshear side than the upshear side but the difference is not statistically significant. We focus on the axisymmetric TCBL structure in this study.

3. Results

a. Characterizing mean PBL kinematic structure as a function of TC intensity

The first task is to establish the fidelity of the composite profile analyses in capturing key characteristics of the TC primary and secondary circulations. This is done by comparing the structures of the azimuthally averaged tangential wind speed ($\langle V_t \rangle$), radial flow ($\langle V_r \rangle$), vertical velocity ($\langle w \rangle$), and divergence ($\langle Div \rangle$) for weak (50 kt $< V_{max} <$ 96 kt) and strong ($V_{max} \geqq$ 96 kt; cf. Fig. 3a) TCs. The $\langle V_t \rangle$ is shown as a function of r^* and z for weak and strong TC groups[1] in Figs. 5a and 5b, respectively. As expected, the maximum value of $\langle V_t \rangle$ is closely

related to the best track storm intensity, consistent with the use of $\langle V_t \rangle$ as an additional measure of storm intensity to the maximum 1-min sustained 10-m wind speed (e.g., Bryan and Rotunno 2009; Zhang et al. 2017b). The peak $\langle V_t \rangle$ at the RMW represents the boundary layer jet that is located at ~500-m altitude in both groups. The radial variation of the height of the maximum $\langle V_t \rangle$ is denoted by the black dashed line in Figs. 5a and 5b, showing an increasing trend with radius.

Composites of azimuthally averaged radial wind ($\langle V_t \rangle$) show that the maximum inflow is located at the lowest vertical level (150 m) of the composites outside the RMW (Figs. 5c,d). Dropsonde composites of Zhang et al. (2011) showed that the maximum axisymmetric inflow is located at 100–200-m altitude, which is consistent with our result. The magnitude of the peak inflow increases with storm intensity in a similar manner to the maximum $\langle V_t \rangle$. The radial location of the peak inflow is outside the RMW, in general agreement with the dropsonde composite of Zhang et al. (2011). The maximum outflow immediately above the inflow layer (i.e., corner flow region; cf. Fig. 2 and associated discussion) also increases with storm intensity, indicating a positive correlation between the peak inflow and outflow strengths. The outflow strength within the corner flow maximizes inside the RMW for all intensity groups. There are two peaks of outflow (at $r^* \sim 1$ and $r^* \sim 2$ in the $z = 1.5$–2-km layer) in the composite of the strong group, with the outer peak likely indicating secondary eyewall or strong outer rainband features outside the RMW.

The frictional inflow layer is denoted by the black solid lines in Figs. 5c and 5d and its depth is taken as the height of 10% of maximum magnitude of negative radial wind (i.e., peak inflow strength) following Zhang et al. (2011). Consistent with the dropsonde composite of Zhang et al. (2011), the Doppler profile composite shows an increase of the inflow layer depth with radius outside the RMW. The height of maximum $\langle V_t \rangle$, indicated by the "x" marks in Figs. 5c and 5d, is within the inflow layer for both strong and weak TCs. Interestingly, both the inflow layer depth and jet height at a given radius outside the RMW are greater in weaker storms. This result may be explained by the dynamical scaling of the boundary layer top in TCs (Kepert 2001; Smith and Montgomery 2020). The boundary layer height (h) is proportional to the square root of the ratio of vertical eddy diffusivity (K_m) to inertial stability (I) in the form of $h = (2K_m/I)^{1/2}$. Previous observational results suggested that the K_m nearly linearly increases with the wind speed (Zhang et al. 2011). However, the inertial stability approximately increases with the square of the wind speed (Zhang and Marks 2015). Thus, the extent of increase in the inertial stability with storm intensity is much larger than the extent of increase in K_m with storm intensity, which in turns leads to a shallower boundary layer for stronger storms. This reasoning may help explain why weaker storms tend to have deeper dynamical boundary layers.

One of the advantages of the Doppler radar profile is that the vertical velocity measurement has much higher radial resolution than dropsondes, which are limited to where dropsondes are released and typically are spaced ~20 km or more apart. Previous dropsonde composite analyses did not include

---

[1] Here, the storm intensity stratification method followed that used in the dropsonde composite analysis of Zhang et al. (2011), except that the weak TC group includes both minor hurricanes and tropical storm strength storms to cover early-stage TCs.
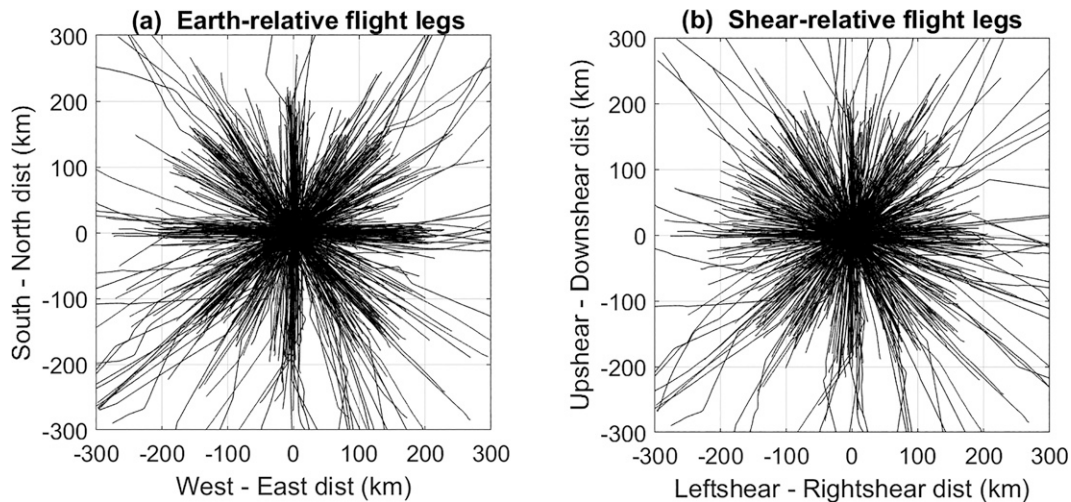
FIG. 4. Horizontal view of radial flight legs in (a) Earth-relative and (b) shear-relative frameworks for all the Doppler profile data. Shear vector in (b) points toward the top of the figure. Note that only data from flights that have more than four radial legs of good data points are included in the composite analysis.

the vertical velocity partly because of this coarse radial coverage. Here, we present the composite of the azimuthally averaged vertical velocity ($\langle w \rangle$) in the TCBL based on the radar profile analyses. This dataset allows us to examine the locations of peak low-level updrafts and their linkage to storm intensity and intensity change. Composites of vertical velocity for the two intensity groups are shown in Figs. 6a and 6b. The maximum composite ascent is located inside the RMW for both groups. This structure is similar to that above the boundary layer in the Doppler swath composites as in Rogers et al. (2012). The magnitude of the peak composite ascent increases with storm intensity, which is consistent with the behavior of both the maximum inflow and outflow flow strengths (cf. Figs. 5c,d) and follows mass continuity.

Composites of azimuthally averaged divergence ($\langle \text{Div} \rangle$) show that the peak radial convergence, as indicated by the negative values in Figs. 6c and 6d, is located at ~150-m altitude (the lowest resolvable level of the profile) and inside the 600-m altitude RMW in both weak and strong TC groups. The magnitude of the peak convergence in the strong group is much larger than that in the weak group, which is consistent with the larger peak vertical velocity below 500 m in the strong group (cf. Figs. 6a,b) by mass continuity.

b. Relationship between mean BL kinematic structure and TC intensity change

In this section, we stratify weak and strong composites of the TCBL kinematic structure into intensifying (INT), steady-state (SS) and weakening (WE) TCs. The INT group includes storms with a future 12-h intensity change greater than or equal to 10 kt. The SS group includes storms with 12-h intensity change between −10 and 10 kt. The WE group includes storms with 12-h intensity change smaller or equal to −10 kt (cf. Fig. 3b). Figure 7 shows the V_t composites for these groups of TCs. The boundary layer jet (at the RMW) is centered at 300–600-m altitude for all three groups, independent

of TC intensity. The height of the maximum V_t is comparable among the intensity change groups for both weak and strong TCs.

The strength of the BL jet is also comparable among the three intensity change groups for both strong and weak TCs (Fig. 7). Both weak and strong TCs are broader outside the RMW in the SS and WE groups than in the INT group, with stronger tangential winds being outside the RMW ($r^* > 2$) for SS and WE TCs. A similar relationship between tangential winds outside the RMW and TC intensity change was found in Rogers et al. (2013). The difference in outer-core winds between intensity change groups is more pronounced for strong TCs. Weak TCs in the WE group have a secondary tangential wind maximum outside the RMW.

INT, SS and WE composites of $\langle V_r \rangle$ in weak and strong TCs are compared in Fig. 8 with the black line showing the top of the inflow layer. In all cases, the TCBL jet denoted by the black x, which has previously been shown to be supergradient (Smith et al. 2009), is located inside the strong inflow layer. The maximum resolved inflow strength in all composites is located at ~150-m altitude above the surface and is located outside the RMW. The peak inflow strength is comparable among the three groups for both weak and strong TCs, with the peak inflow being largest near the RMW in the INT group. Interestingly, the radial location of the peak inflow shifts farther outward from the RMW as the intensification rate decreases (from INT to SS, and then to WE).

The peak outflow strength inside the RMW is weaker in the SS and WE groups than in the INT group, especially for strong TCs. The INT composite has weak inflow above the frictional layer outside the RMW. However, there are secondary outflow peaks outside the RMW (between $r^* = 1.5$ and 2.5) above the inflow layer in both SS and WE groups of both weak and strong TCs, which is not obvious in the INT group. The inflow layer depth is larger in weak TCs than in strong TCs for all three intensity change groups. Interestingly, the inflow layer
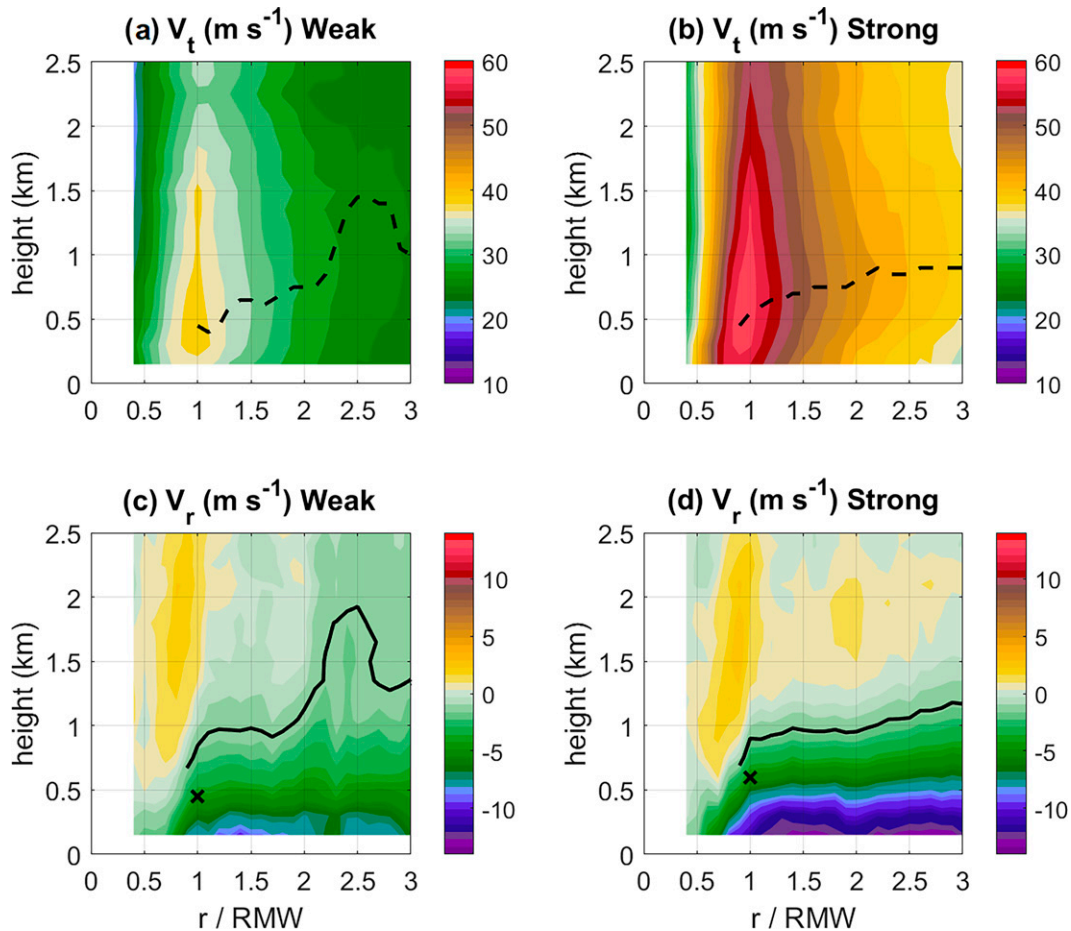
FIG. 5. Plots of composite axisymmetric tangential wind (V_t) for (a) weak and (b) strong tropical cyclones (TCs), and composite axisymmetric radial wind (V_r) for (c) weak and (d) strong TCs as a function of normalized radius (r/RMW_{600m}) and height. The weak group is for storms with intensity between 50 and 96 kt, while the strong group is for storms with intensity greater than 96 kt. The black dashed line in (a) and (b) represents the height of the maximum V_t. The thick black line in (c) and (d) represents the inflow layer depth defined as the height of 10% maximum inflow. The black x mark in (c) and (d) shows the location of maximum V_t.

outside the RMW is much deeper in the INT group than in both SS and WE groups of weak TCs.

The INT, SS, and WE composites of $\langle w \rangle$ in both weak and strong TCs show the peak updraft inside the 600-m RMW with a relatively small difference in strength for weak TCs (Fig. 9). Convection, inferred from deep regions of composite ascent, is primarily concentrated near the RMW in the INT composite (Figs. 9a,d). This result suggests that stronger inflow near the RMW associated with intensifying TCs (cf. Figs. 8a,d) organizes convection more inside the RMW during intensification, while the stronger inflow outside the RMW in steady-state or weakening TCs is tied to more convective activity in the outer core region. Differences in the radial location of peak updraft inside the RMW are insignificant among the three intensity change groups for both weak and strong TCs.

A clearer signal between vertical velocity and intensity change is seen outside the RMW, where there is greater composite azimuthal-mean ascent within $r^* = 2$–3, reflecting more convective activity in the SS and WE groups than in the INT group for both weak and strong TCs. The convective activity in WE cases is even less focused than in the steady state cases, as indicated by more radially expanded updraft peaks. This result suggests that the radial distribution and coverage of convective activity outside the RMW is tied to TC intensity change.

c. Relationship of mean TCBL kinematic structure to vortex-scale structure

The results shown in the previous subsection have highlighted differences in TCBL structure that are related to TC intensity change, including the shape of the tangential wind field, the peak inflow strength and location, the depth of the inflow layer, and the strength and radial distribution of peak updrafts. Here we focus on one aspect of vortex structure, the shape of the tangential wind field just above the TCBL, to investigate its relationship to the TCBL flow structure.
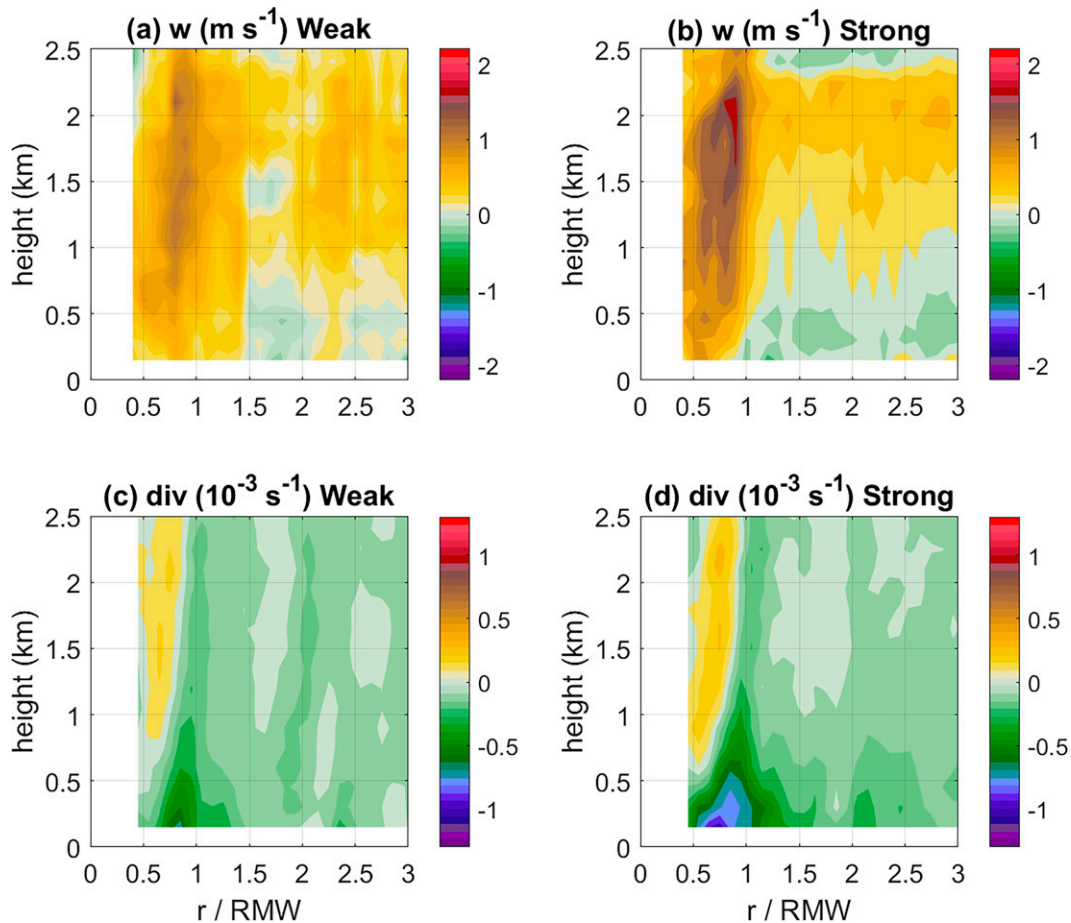
FIG. 6. Plots of composite axisymmetric vertical wind (w) for (a) weak and (b) strong tropical cyclones (TCs), and composite axisymmetric divergence (div) for (c) weak and (d) strong TCs as a function of normalized radius (r/RMW$_{600m}$) and height. The weak group is for storms with intensity between 50 and 96 kt, while the strong group is for storms with intensity greater than 96 kt.

Composite analyses of Doppler swath data in TCs have shown that broader vortices with higher outer-core inertial stability have reduced inflow above the TCBL, implying a linkage between the midlevel inflow with the inertial stability in a balanced vortex (Rogers et al. 2013). A recent study by Smith and Montgomery (2020) discussed how some previous studies have wrongly invoked this idea of radial flow resistance with greater outer-core inertial stability in the TCBL. In this section, we evaluate the TCBL kinematic structural differences for storms with different vortex structures, as defined here in terms of the radial decay rate of tangential wind, and explore its relationship with TC intensity change.

1) PBL STRUCTURE IN NARROW AND BROAD VORTICES

We composite the Doppler profile data for narrow and broad vortex profiles above the inflow layer (1.5-km altitude) outside the RMW, as shown in Fig. 10a. There are ~30 flights for both the narrow and broad composite profiles, defined as the upper and lower 33% of the total samples of the radial

rate of tangential wind decay, respectively. Note that each individual radial profile of tangential wind is an average of all profile data for a given flight. The narrow vortex has a smaller inertial stability outside the RMW ($r^* > 2$) than the broad vortex (Fig. 10b).

Differences in the maximum $\langle V_t \rangle$ at 1.5-km altitude (and associated best track intensity, cf. Table 2) are not statistically significant in the narrow and broad vortex groups. However, the narrow vortices intensified while the broad vortices weakened, as the average 12-h intensity change for the narrow (broad) vortex group is 5.2 kt (-2.5 kt). Differences in sea surface temperature (SST), midlevel environmental moisture, and environmental shear magnitude and direction between the narrow and broad groups are not statistically significant at the 95% confidence level (Table 2), indicating that the differences in intensity change values between broad and narrow vortices are not explained by these environmental parameters.

Composites of $\langle V_t \rangle$ within and above the TCBL for the narrow and broad vortex groups are shown in Figs. 11a and 11b, respectively. Peak values of $\langle V_t \rangle$ are comparable between the
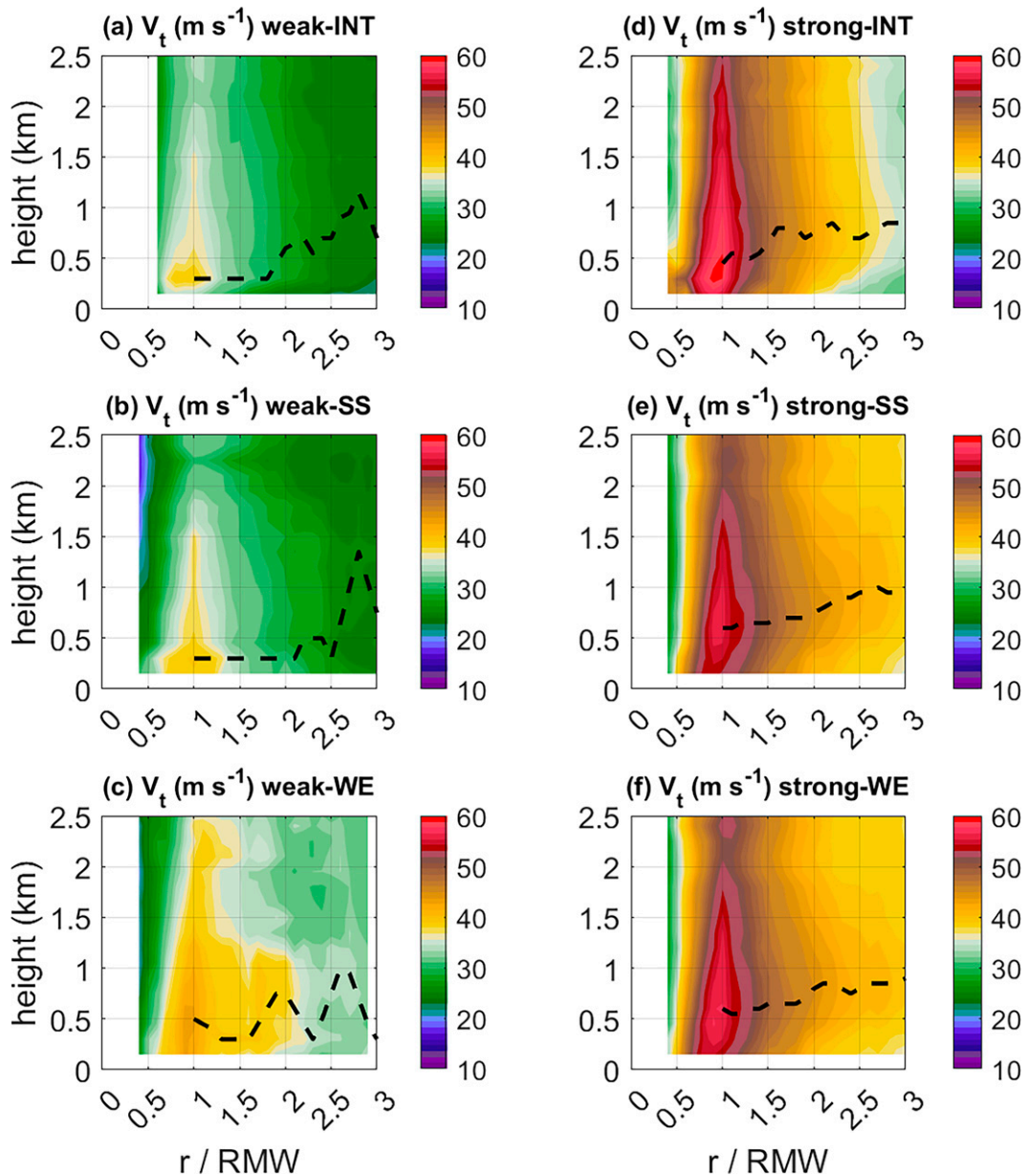
FIG. 7. Plots of composite axisymmetric tangential wind (V_t) for (a) intensifying (INT), (b) steady-state (SS), and (c) weakening (WE) weak tropical cyclones (TCs), and that for (d) INT, (e) SS, and (f) WE strong TCs as a function of normalized radius (r/RMW$_{600m}$) and height. The INT group is for storms with a future 12-h intensity change larger than 10 kt; the SS group is for storms with future 12-h intensity change magnitudes less than 10 kt; and the WE group is for storms with a future 12-h intensity change less than −10 kt. The black dashed line in each panel represents the height of the maximum V_t.

two datasets, but the difference field in Fig. 11c clearly shows the structural differences between the narrow and broad vortices. The jet height at the RMW ($r^* = 1$) is also located at a higher altitude in the narrow vortex than in the broad vortex.

The radial flow field for each vortex structure is shown in Figs. 11d and 11e. While the peak inflow values are comparable for the different vortex types, the radial location of the peak inflow is substantially different. The peak inflow is located right outside the RMW (1–1.5r^*) in the narrow vortex (Fig. 11d), while it is located at the outer radii (2.5–3r^*) in the broad vortex (Fig. 11e). Given that the inertial stability is larger outside the RMW in the broad vortex than in the narrow vortex (Fig. 10b), this result indicates that the strength of the peak inflow in the frictional inflow layer is not purely correlated with the inertial stability. This result is consistent with the finding of Smith and Montgomery (2020), based upon the
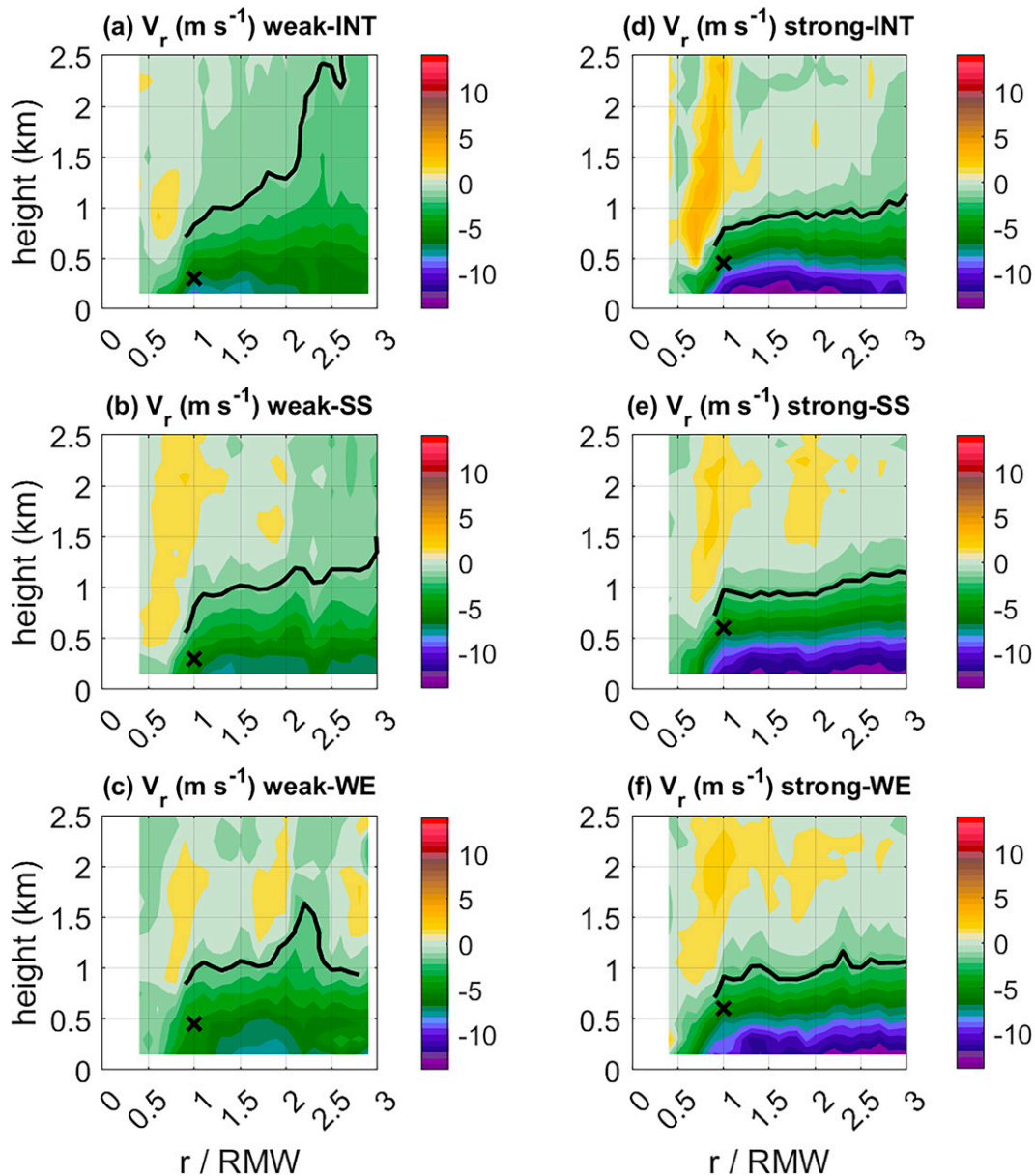
FIG. 8. As in Fig. 7, but for the composites of axisymmetric radial wind (V_r). The thick black line represents the inflow layer depth. The black x shows the location of maximum V_t.

linear generalized Ekman model, that the peak inflow at any radius within the PBL is not correlated with the inertial stability.

On the other hand, the radial flow does appear to be negatively correlated with the inertial stability above the inflow layer ($z > 1$ km), which shows regions of weak (1–2 m s^{-1}) inflow for narrow vortices and near-zero inflow, and even weak outflow, for broad vortices (Figs. 11d,e). Inflow above the TCBL for narrow vortices suggests that convection within the eyewall is generally more than sufficient to ventilate the air exiting the TCBL, so that air above the TCBL is drawn inward to satisfy mass continuity (Kilroy et al. 2017a; Smith et al.

2021). In contrast, outflow outside the RMW above the TCBL for broad vortices may in part (see below) indicate an inability of eyewall convection to ventilate the mass exiting the TCBL, resulting in weak outward flow above the TCBL. This outflow is likely associated with an outer updraft induced by an outer rainband or secondary eyewall.

As mentioned above, the main difference in radial flow in the friction layer between the two vortex types is in the radial location of the peak frictional inflow outside the RMW. The broad vortex has a larger near-surface ($z < 500$ m) inflow in the outer core region ($r^* > 2.5$), while the narrow vortex has a larger near-surface inflow near the RMW ($1 < r^* < 1.5$;
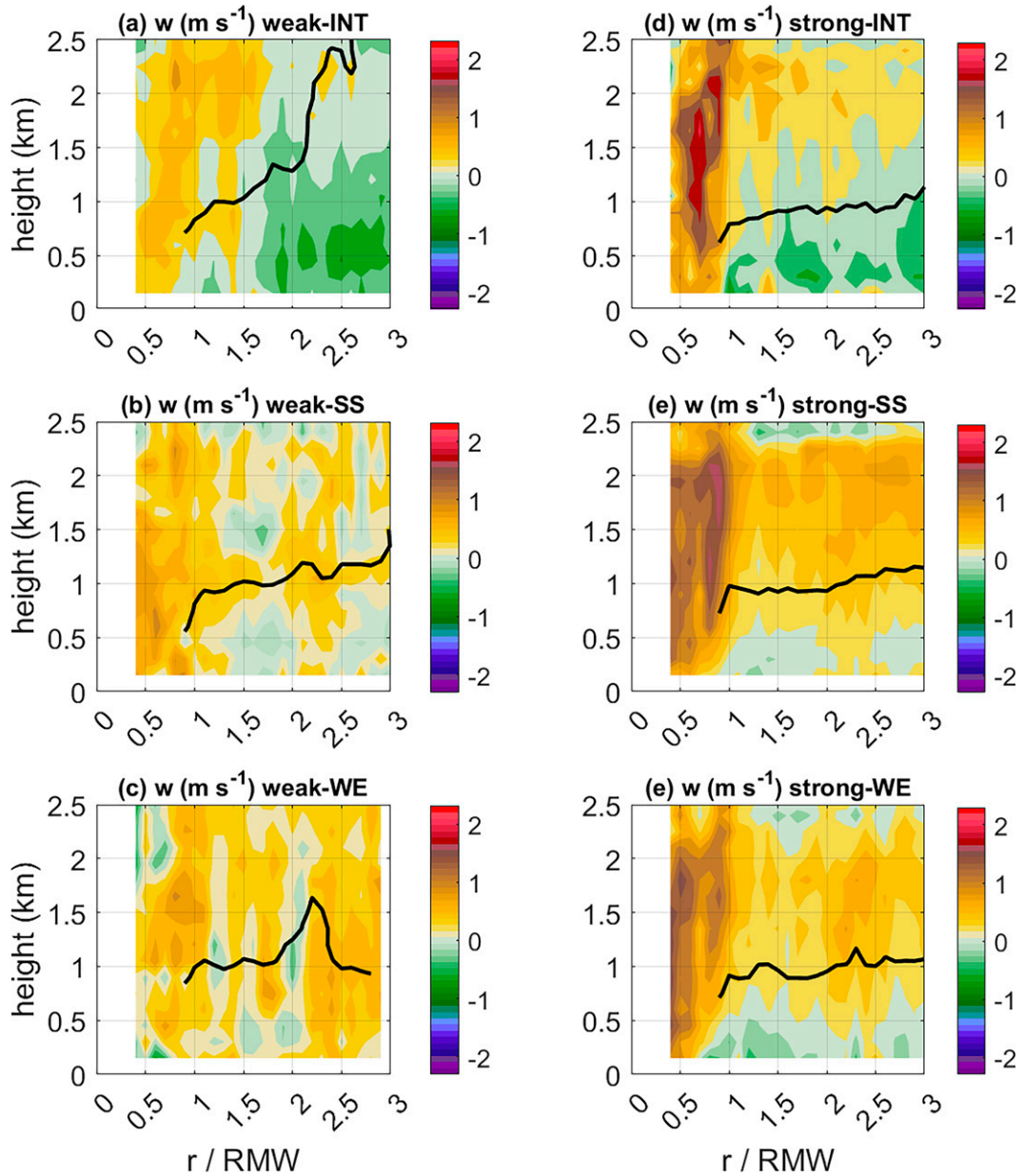
FIG. 9. As in Fig. 7, but for the composites of axisymmetric vertical wind (w). The thick black line represents the inflow layer depth.

Figs. 11d,e). The $\langle V_r \rangle$ difference pattern, significant at the 95% confidence level, extends up to ~1-km altitude (Fig. 11f). Figures 11d and 11e also show that the inflow layer is deeper in the narrow vortex than in the broad vortex.

Composites of $\langle w \rangle$ show stronger and deeper maximum ascent inside the RMW in the narrow vortex than in the broad vortex (Figs. 12a–c). This result is also quantitatively consistent with the composite results of INT versus SS (or WE) TCs shown in the previous section, as the narrow vortex TC on average intensifies while the broad vortex TC weakens. The local maximum in ascent immediately above the inflow layer ($z \sim 0.5$ km) is significantly larger for the narrow vortex

(Fig. 12c). The radial location of the maximum ascent inside the RMW is comparable in the narrow and broad vortices. Kepert (2017) pointed out that the inward displacement of forced ascent from the RMW (δR) is proportional to the ratio of the near-surface (10-m) maximum inflow magnitude to the inertial stability above the BL [max($|V_r|$)/I] based on a dynamical scaling. Our $\langle V_r \rangle$ composites (Figs. 11d,e) and radial profiles of inertial stability (Fig. 10) suggest that this ratio near the RMW of the narrow vortex is larger than that of the broad vortex. However, the difference in δR between the narrow and broad vortices is small, which is a surprising but interesting result when compared to this dynamical scaling.

(a) normalized tangential wind speed (V_t)

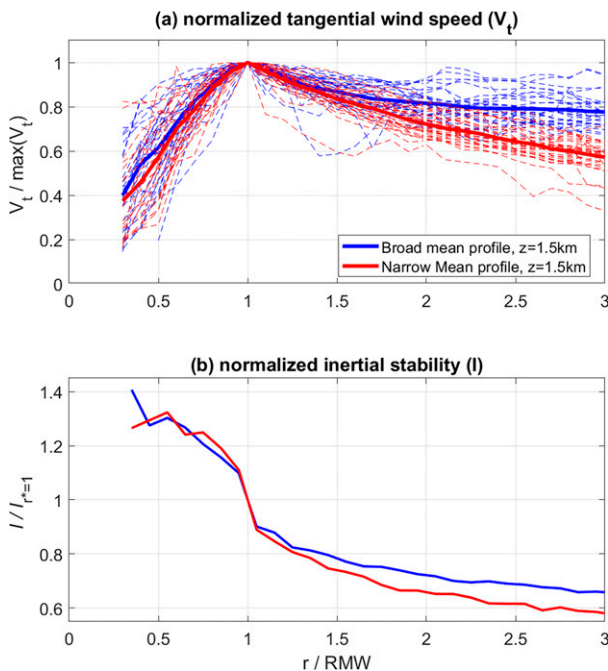## (b) normalized inertial stability (I)

FIG. 10. (a) Plot of axisymmetric tangential wind (V_t) at 1.5-km altitude normalized by its maximum as a function of normalized radius (r/RMW) and (b) plot of inertial stability (I) calculated using the mean wind profile normalized by its value at the RMW as a function of r/RMW. RMW is the radius of the maximum tangential wind speed.

It was noted by Kepert (2017) that small storms tend to have smaller δR, which may partly explain the relatively small difference in δR between two types of vortices, as narrow TCs overall have smaller RMWs despite larger max($|V_r|$)/I. Above all, our profile composites (Figs. 7–12) indicate that δR in the eyewall region is not tied to the TC intensity change.

These $\langle w \rangle$ composites suggest that there is significantly more convective activity outside $r^* = 1.5$ for the broad vortex than the narrow vortex (Figs. 12a,b), indicating outer rainbands or secondary eyewalls are more frequent for the broad vortex. This result agrees with the findings of $\langle w \rangle$ composites of INT versus SS (or WE) groups, in that intensifying (narrow) TCs tend to have more concentrated convective activity close to the RMW than steady-state/weakening (broad) TCs. Greater convective activity at $r^* > 1.5$ for the broad vortex also may help explain differences in radial flow structure above the TCBL noted previously (cf. Figs. 11d,f). The balanced secondary circulation associated with outer-core convection is a likely source of outflow above the TCBL for the broad vortex (Fig. 11e). This

outflow is in addition to that potentially resulting from an inability of eyewall convection to ventilate air flowing out of the boundary layer for broad TCs as discussed earlier.

The peak convergence is located near the surface inside the RMW in both composites (Figs. 12d,e). However, the magnitude of the peak convergence is statistically significantly larger for the narrow vortex (Fig. 12f). This result is tied to the difference in TCBL inflow structure between the two vortices, and it indicates that storms with stronger convergence tend to intensify faster, given that the narrow TC group intensifies while the broad TC group weakens. The stronger peak convergence is consistent with the stronger azimuthal-mean ascent for narrow vortices mentioned earlier, indicating a greater evacuation of mass from the BL in the narrow vortex. This result also supports the findings of TCBL inflow composites of INT, SS and WE groups in the previous section. Although not statistically significant, the outer-core ($r^* > 2$) convergence within the TCBL for the broad vortex is larger than that for the narrow vortex. Prior studies have shown a relationship between enhanced TCBL convergence in the outer core and the presence of organized convection there. For example, Rogers et al. (2016; their Figs. 11 and 12) showed that weakening Hurricane Edouard exhibited maximum convergence outside the RMW where convection developed according to the Doppler swath data, consistent with our findings based on profile composites. Modeling studies have also suggested a coupling of processes above the BL and the TCBL dynamics during secondary eyewall development (Rozoff et al. 2008; Huang et al. 2012; Kepert 2013; Montgomery et al. 2014b; Kepert and Nolan 2014).

2) MEAN ADVECTION OF ABSOLUTE ANGULAR MOMENTUM

As mentioned earlier, theoretical studies (e.g., Smith et al. 2009) pointed out that an agradient force acts to spin up a storm if the total advection of absolute angular momentum (M) is larger than the reduction of M by frictional torque. The M budget equation is shown below:

$$\frac{\partial \langle M \rangle}{\partial t} = -\langle V_r \rangle \frac{\partial \langle M \rangle}{\partial r} - \langle w \rangle \frac{\partial \langle M \rangle}{\partial Z} - \left\langle V_r' \frac{\partial M'}{\partial r} \right\rangle$$
$$- \left\langle w' \frac{\partial M'}{\partial Z} \right\rangle + F_r. \tag{11}$$

Here $M = rV_t + 1/2fr^2$, where r is radius and f is the Coriolis frequency. The bracket represents an azimuthal average at each vertical level, and the prime represents a deviation from the azimuthal mean (i.e., a perturbation or "eddy"). Terms on

TABLE 2. Comparison of parameters for the Doppler profile composites of the narrow and broad vortices. Here, V_{max} is the storm intensity, INT12h is the 12-h intensity change, RMW is the radius of the maximum wind speed at 600-m altitude, SST is the sea surface temperature, shearMag represents 850–200-mb shear magnitude, shearDir is the shear heading, and RHMD is the midlevel environmental relative humidity.

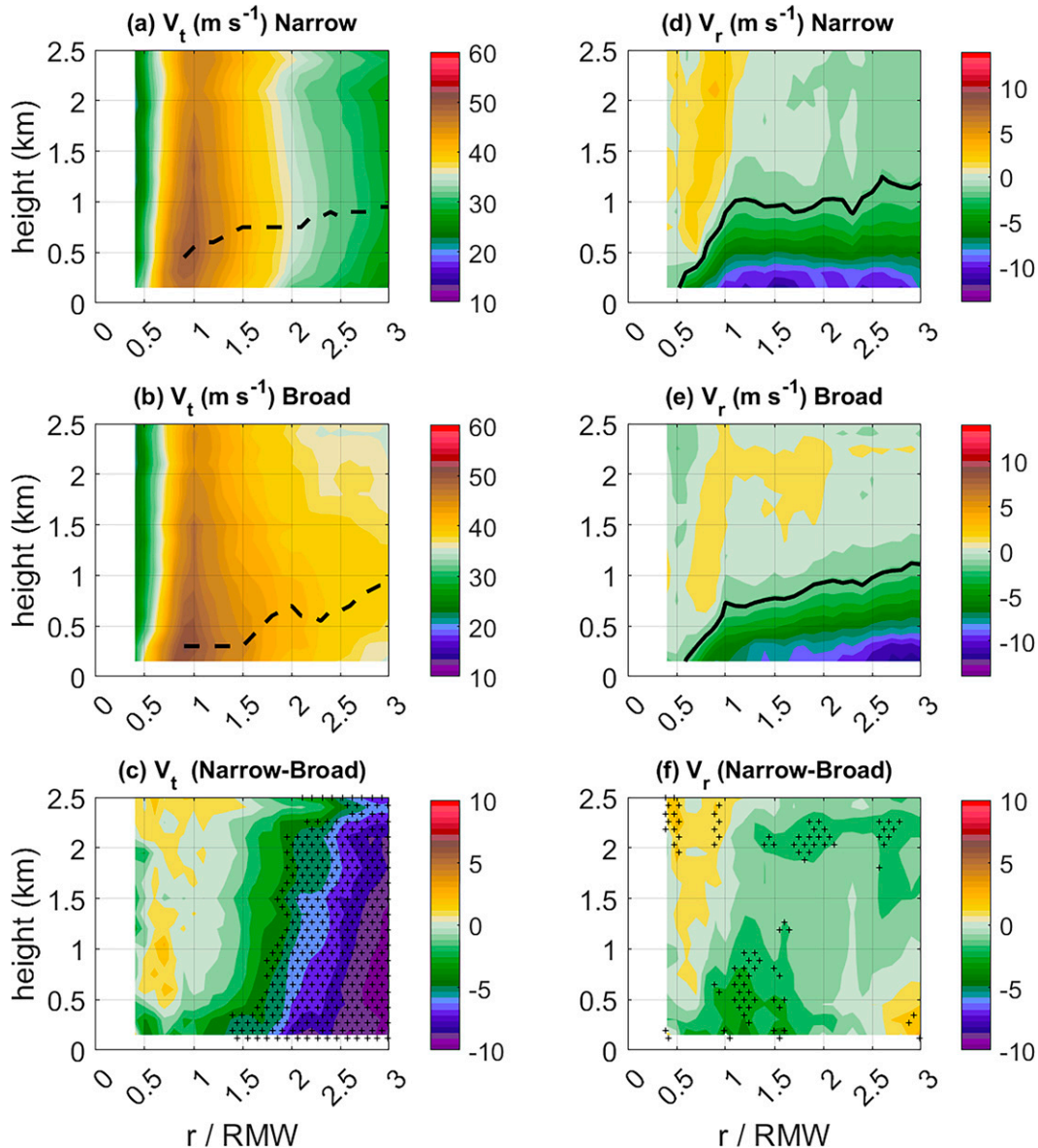| Vortex type	V_{max} (kt)	INT12h (kt)	RMW (km)	SST (°C)	ShearMag (kt)	shearDir (°)	RHMD (%)
Narrow	99.7	5.2	27.6	29.0	13.7	102.9	55.9
Broad	100.3	−2.5	30.9	29.2	14.4	116.7	50.3

FIG. 11. Plots of composite axisymmetric tangential wind (V_t) for (a) narrow and (b) broad vortices, and axisymmetric radial wind (V_r) for (d) narrow and (e) broad vortices as a function of normalized radius ($r/\mathrm{RMW}_{600\mathrm{m}}$) and height. The difference field is shown in (c) and (f) for V_t and V_r, respectively. The black + symbols in (c) and (f) labels where the difference is statistically significant at 95% confidence level. The black dashed line in (a) and (b) represents the height of the maximum V_t. The black solid line in (d) and (e) represents the inflow layer depth.

the right-hand side of Eq. (11) represent the mean radial advection of $\langle M \rangle$, the mean vertical advection of $\langle M \rangle$, the radial eddy transport of $\langle M \rangle$, the vertical eddy transport of $\langle M \rangle$, and the frictional dissipation term[2] (F_r), respectively.

Using the composited wind fields, the mean advection terms in the M budget for the broad versus narrow vortex are

evaluated. The eddy advection and friction terms cannot be reliably estimated from the Doppler profile dataset since eddy quantities are only available along a few radial flight legs sampled over a several hour period, and thus the azimuthal mean of products of eddy quantities would not be meaningful. This is not considered a significant problem, though, because the magnitude of the total eddy term is generally small (5%–15%) compared to the mean advection term (Persing et al. 2013; Smith et al. 2017; Leighton et al. 2018; Zhang and Rogers 2019). The high wavenumber eddy terms may be estimated using the Imaging Wind and Rain Airborne
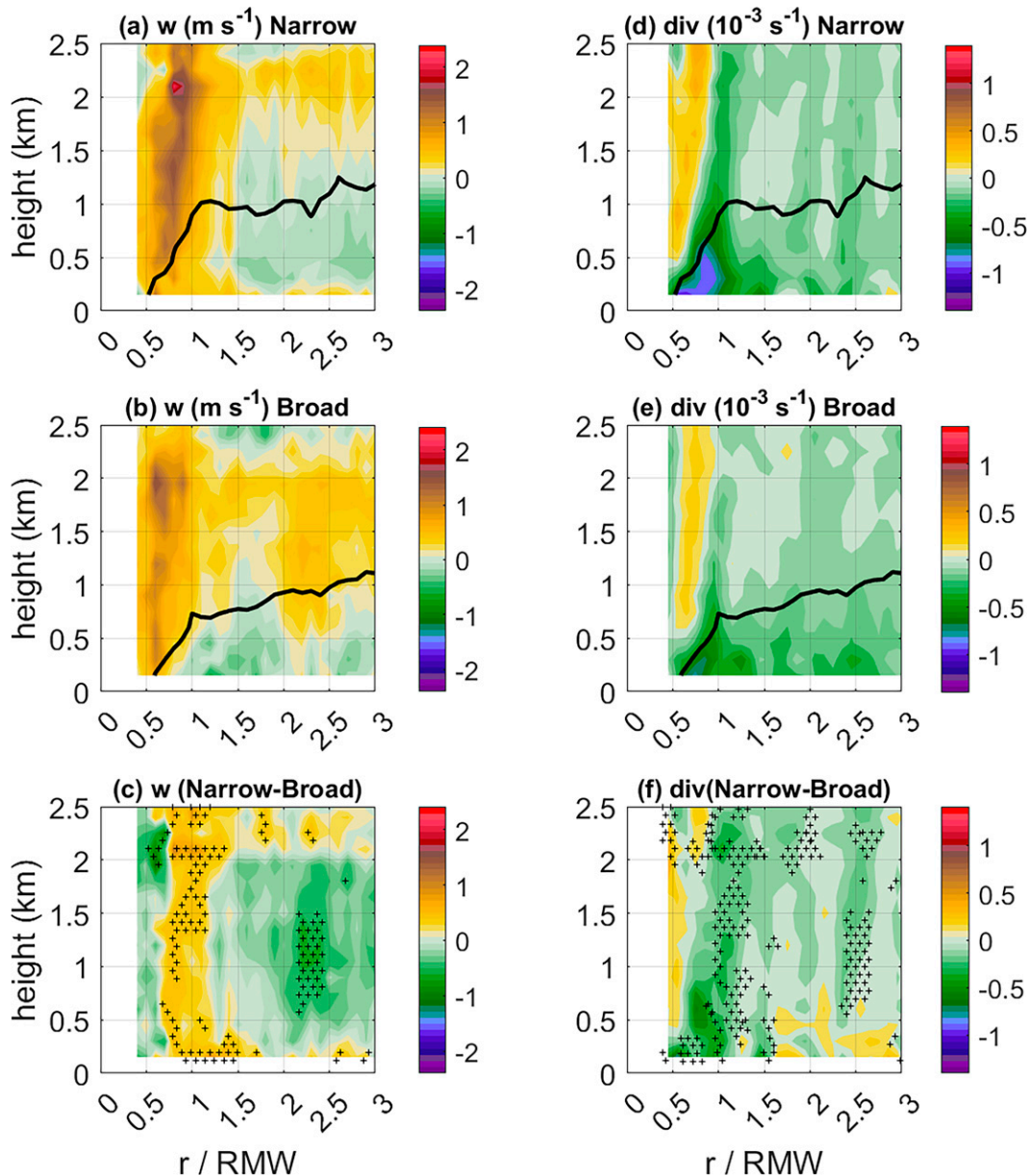
---

[2] The frictional dissipation term includes both frictional dissipation of momentum near the surface and sub-grid turbulent diffusion of momentum (e.g., Persing et al. 2013; Smith et al. 2017; Zhang and Rogers 2019).

FIG. 12. Plots of composite axisymmetric vertical wind (w) for (a) narrow and (b) broad vortices, and divergence (div) for (d) narrow and (e) broad vortices as a function of normalized radius (r/RMW_{600m}) and height. The difference field is shown in (c) and (f) for w and div, respectively. The black + symbols in (c) and (f) labels where the difference is statistically significant at the 95% confidence level. The black solid line represents the inflow layer depth.

Profiler[3] (IWRAP) data that has a larger azimuthal coverage and resolution than the profile data in the boundary layer (Guimond et al. 2020). Such an analysis is beyond the scope of the present study, however.

Nonetheless, previous studies have shown that an axisymmetric perspective of the three-dimensional physical processes

associated with TC intensity change can prove useful (e.g., Smith et al. 2021). The mean advection terms in the M budget are evaluated here to provide insight into the first-order contributions to TC intensification and, specifically, why the two types of vortex structure are associated with different intensification rates. A similar approach was followed in Zhang et al. (2017b), who compared the mean advection of M in HWRF forecasts of RI and non-RI cases related to PBL physics differences. They found that the mean advection of M close to the RMW was significantly larger in the RI cases than in the non-RI cases, although the mean storm intensity of the two groups was not

---

[3] Note that the resolution of the IWRAP data is much higher than the profile data and thus provides significant advancements in the understanding of the turbulent TCBL structure (Guimond et al. 2018, 2020; Sroka and Guimond 2021).
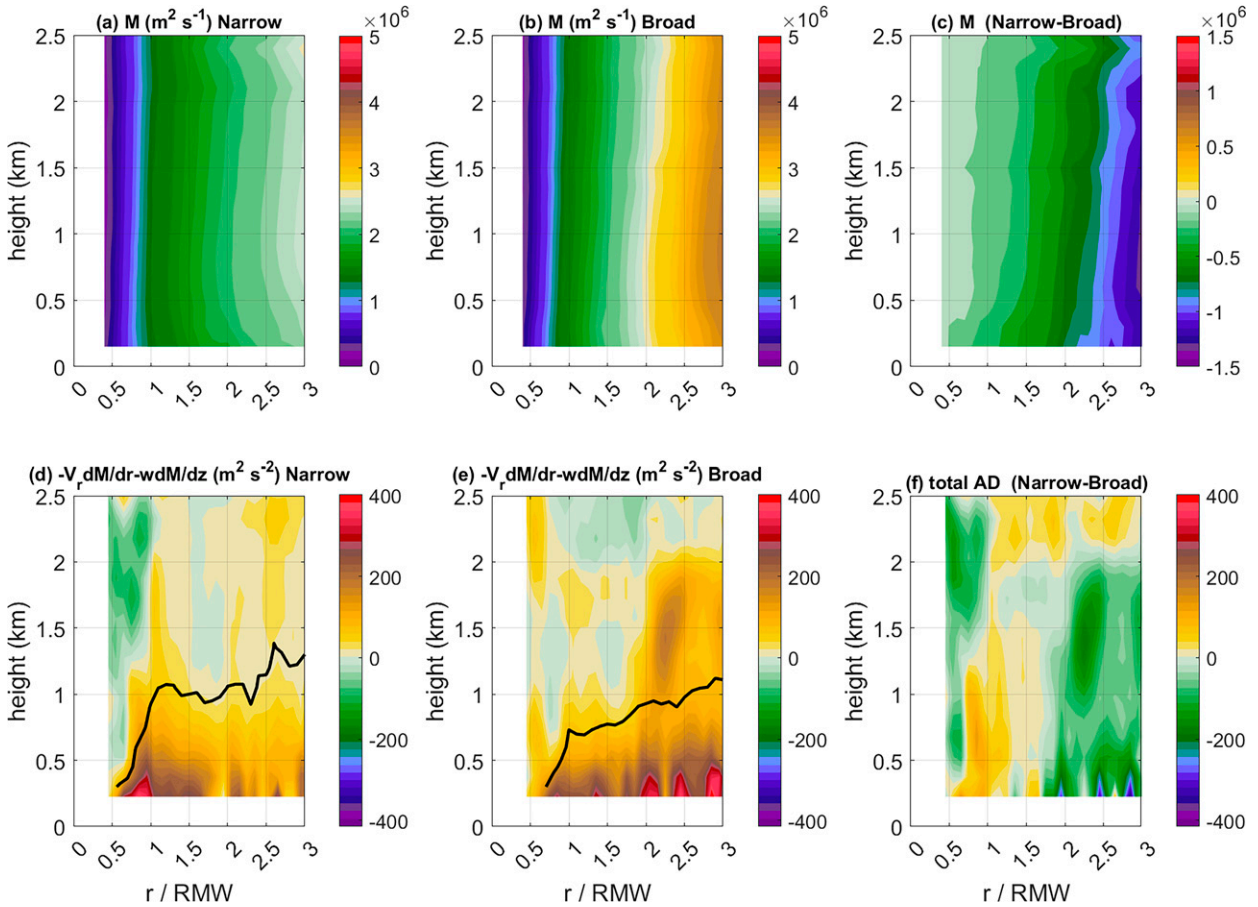
FIG. 13. Plots of composite axisymmetric absolute angular momentum (M) for (a) narrow and (b) broad vortices, and total advection of M (total AD $= -V_r dM/dr - wdM/dz$) in the M budget for (d) narrow and (e) broad vortices as a function of normalized radius (r/RMW$_{600m}$) and height. The difference field is shown in (c) and (f) for M and total AD, respectively. The black line denotes the inflow layer depth.

significantly different. Here, we document the structure of the momentum advection terms that arises based on the observed TCBL wind structure, which may provide a reference for future modeling studies to infer whether a simulated structure is realistic or not.

The $\langle M \rangle$ composites show larger values of M outside the RMW in the broad vortex than in the narrow vortex (Figs. 13a–c), consistent with the $\langle V_t \rangle$ comparison result[4] in Fig. 11 and Table 2. The total mean advection of M is compared between the narrow and broad vortices in Figs. 13d and 13e with the difference field shown in Fig. 13f. The total mean advection of M is positive below ~1-km altitude in both narrow and broad vortices, indicating a positive contribution of this term to the M tendency. The maximum M advection is larger near the RMW in the narrow vortex than in the broad vortex, consistent with the stronger inflow just outside the RMW (cf. Figs. 11d and 11e). This difference indicates a faster

spinup for the narrow vortex, assuming that the friction term is comparable for the two vortex profiles. Close to the RMW and below 1.5-km altitude, the positive total advection of M is larger in the narrow vortex, suggestive of a faster spinup of the narrow vortex there. However, the total advection of M below 2-km altitude and at $r^* > 2$ is much larger in the broad vortex than in the narrow vortex, consistent with the stronger inflow and upward motion for broad vortices at those radii (cf. Figs. 11 and 12) and suggestive of the development of a secondary eyewall or rainbands in this region.

Figure 14 separates the contributions to the total mean advection of M into its radial and vertical components. The spinup of both vortices in the inflow layer contributed by the positive total advection of M mainly comes from the radial advection of M, as the vertical advection negatively contributes (although to a small extent) to the M tendency (Figs. 14a,b,d,e). The negative radial advection of M inside the RMW resulting from the outflow is fully offset by the vertical advection in both vortices such that the positive total mean advection extends above the inflow layer (cf. Figs. 13d and 13e). The magnitude of the radial advection near the RMW in the inflow

---

[4] Since the mean RMW for the broad vortices is only about 3 km greater than the narrow vortices (cf. Table 2), the M difference is mainly due to the V_t difference.
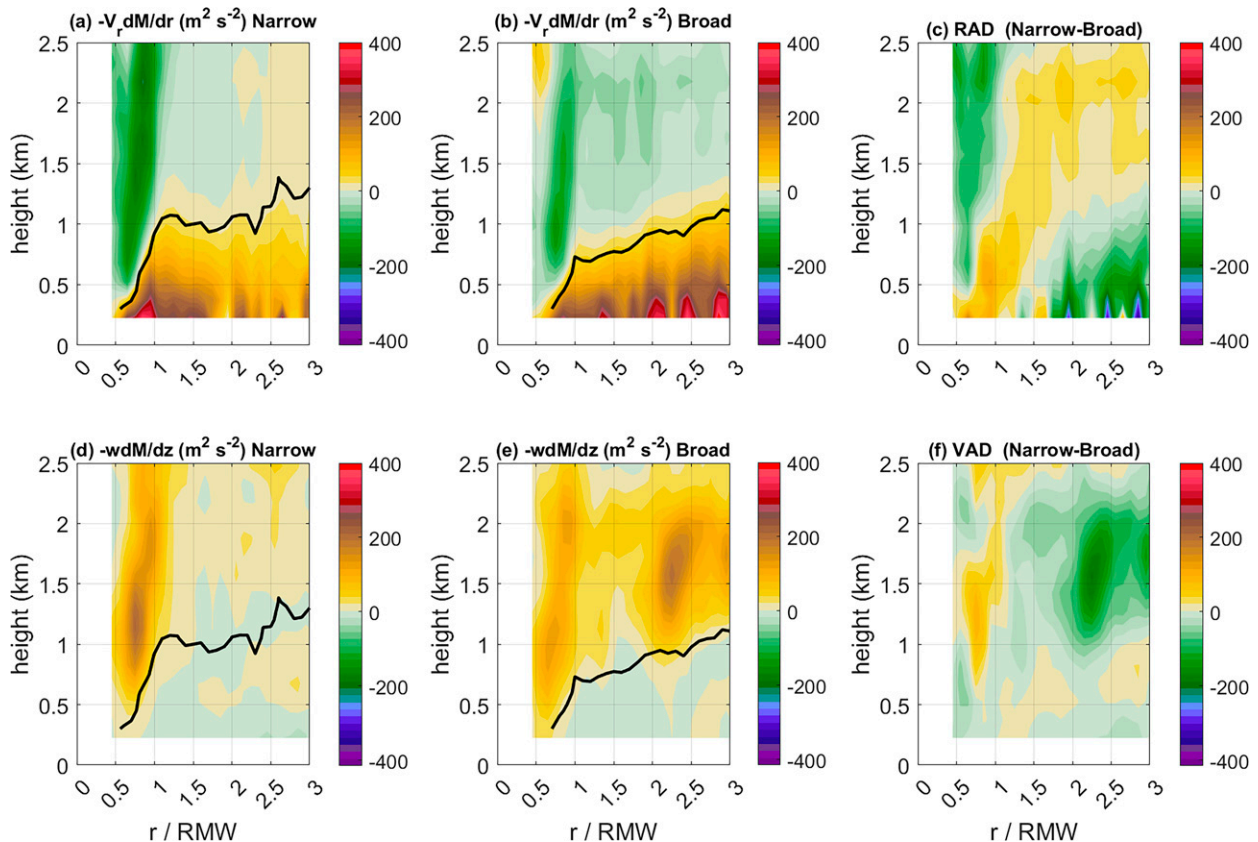
FIG. 14. Plots of radial advection of absolute angular momentum (RAD = $-V_r dM dr$) for (a) narrow and (b) broad vortices, and vertical advection of M (VAD = $-wdM/dz$) for (d) narrow and (e) broad vortices as a function of normalized radius (r/RMW$_{600m}$) and height. The difference field is shown in (c) and (f) for RAD and VAD, respectively. The black line represents the inflow layer depth.

layer is larger in the narrow vortex than in the broad vortex, while the radial advection magnitude is larger at $r^* > 2$ in the broad vortex (Fig. 14c). A similar result is seen in the comparison of vertical advection there (Fig. 14f), but the largest difference is near the top of the inflow layer (1–2-km altitude). In the outer-core region, the spinup of the broad vortex above the inflow layer is mainly contributed by the vertical advection of M (Fig. 14e).

4. Discussion and conclusions

This study investigates the characteristics of azimuthally averaged TCBL kinematic structure in TCs using airborne Doppler radar profile data. Composites of the TCBL structure were conducted for TCs of different intensity, intensification rate and radial structure. As expected, strong storms have stronger peak inflow, larger maximum tangential wind speed, stronger ascent inside the RMW, and stronger boundary layer convergence than weak storms. The maximum tangential wind speed is within the frictional inflow layer in both weak and strong TCs. Results also showed that the TCBL is deeper in weak storms than in strong storms, which is quantitatively consistent with theory (Kepert 2001; Zhang et al. 2015).

When considering the structure of the TCBL and its relationship with TC intensity change, it was found that the tangential wind is stronger outside the RMW in both steady-state and weakening TCs compared with intensifying TCs for both weak and strong cases, a result consistent with past studies. The inflow layer outside the RMW is deeper in intensifying storms than in steady-state or weakening storms, especially for weak TCs. Although the peak inflow strength is comparable among the three intensity change groups, the peak inflow near the surface is located farther away from the RMW as the storm intensification rate decreases. Secondary outflow peaks were observed outside the RMW in SS and WE TCs, while they do not appear in INT TCs. Convective activity, as inferred from the azimuthal mean of vertical velocity, is more concentrated close to the RMW in intensifying TCs, while convective activity indicative of outer rainbands or secondary eyewalls is evident in steady-state and weakening TCs.

Focusing on the differences in the TC outer-core tangential wind field above the inflow layer (i.e., broad versus narrow vortices) yielded perhaps the most noteworthy differences in TCBL structure and its relationship to TC intensity change. These differences are summarized by a schematic diagram in Fig. 15. Our results showed that,
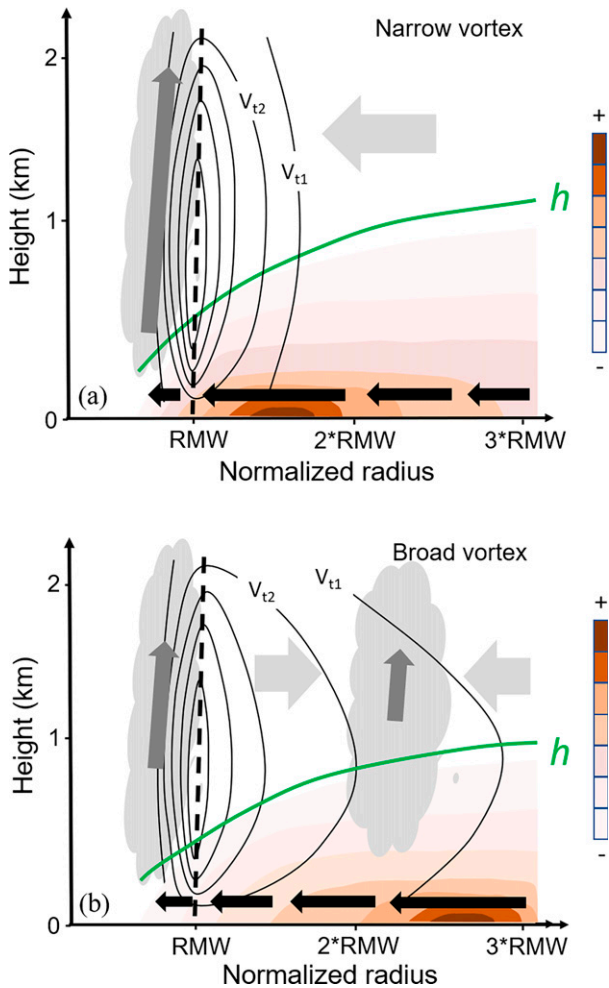
FIG. 15. Schematic showing differences in radial flow and vertical velocity for (a) narrow and (b) broad vortex. Black contours denote tangential wind [values arbitrary, but labels V_{t1} and V_{t2} represent same values in (a) and (b) and peak tangential wind not less than 40 m s^{-1}]. Red shaded contours denote radial wind (values arbitrary, but darker shades denote stronger radial flow). Thick black arrows denote frictionally driven radial inflow; thick medium gray arrows and cloud symbols denote updrafts arising from the BL of the primary eyewall in (a), and from the BL of both primary eyewall and secondary maximum in (b); the thick light gray arrows denote radial flow above the friction layer. The lengths of all thick arrows scale to the magnitude of flow. The green line denotes depth of frictional inflow (h).

compared to broad vortices, narrow vortices have the following characteristics:

- Deeper inflow layer
- Stronger inflow just outside the RMW ($1.0 < r^* < 1.5$)
- Stronger convergence and ascent inside the RMW
- Little to no convective activity outside the RMW
- Weaker inflow and convergence outside the RMW ($r^* > 2.0$)

Insight into the observed differences in TCBL structure for broad and narrow tangential wind profiles above the inflow layer may be possible through comparison with idealized

modeling studies like Smith and Montgomery (2020). In their study of steady-state TCBL structure employing the linear generalized Ekman model, relatively narrow vortex profiles yielded a deeper inflow layer than much broader vortices, with stronger peak inflow outside the RMW and corresponding stronger outflow just above. Both narrow and broad vortex solutions exhibited peak inflow near $r^* = 2$–2.5. Interestingly, at larger radii ($r^* > 4$) their broader vortex showed stronger inflow due to a slower decay of the radial flow with increasing radius, a result they argued would not arise if TCBL inflow was controlled primarily by inertial stability. Similarly, our narrow vortex composite exhibits stronger and deeper inflow just outside the RMW (peak values at $r^* \sim 1.5$) when compared to the broad vortex composite. The broad vortex also exhibits stronger composite radial inflow well outside the RMW ($r^* > 2.5$) than the narrow vortex. The aforementioned magnitude differences in radial inflow between broad and narrow TCs, however, arise due to the substantial differences in radial location of peak inflow. This and the presence of a secondary maximum in azimuthal mean ascent for broad vortices point to rainband activity and secondary eyewalls—structures not simulated by Smith and Montgomery. Further work, therefore, is needed to determine the extent to which torque-balance concepts based on linear theory may help explain the sensitivities of TCBL structure to the gradient vortex profile above, or if it requires a nonlinear theory that includes the effect of outer-core diabatic heating to reproduce the observed difference in the TCBL between narrow and broad vortices.

Given that the key environmental parameters (e.g., SST, shear, and midlevel humidity) are not statistically significantly different between the broad and narrow vortex groups, vortex-scale properties (e.g., the radial decay rate of the tangential wind profile outside the RMW) may play an important role in modulating TC intensity. Understanding the sensitivity of short-term (~12-h) intensification to vortex profile may be approached using the framework of boundary layer control and ventilation recently articulated by Smith et al. (2021). Here, ventilation refers to the capacity of eyewall convection to transport the air mass erupting out of the TCBL. If the convective mass flux in the eyewall region, for example, exceeds the mass flux at the top of the TCBL, then air radially outside the eyewall will tend to be drawn in above the TCBL. This scenario is depicted in Fig. 15a for the narrow (intensifying) vortex. Although we did not explicitly compute the vertical mass flux through the lower- to middle-troposphere, we may infer that it was sufficiently large to ventilate the mass exiting the TCBL given the outer-core inflow above the TCBL documented here. The relatively low outer-core inertial stability of the narrow vortex permitted the inflow above the TCBL to penetrate well into the core region ($r^* \sim 1.5$–2). The corresponding inward radial advection of angular momentum contributed to a net positive symmetric spinup tendency in this region. According to the concept of boundary layer control (Kilroy et al. 2016; Kilroy et al. 2017a,b), the TCBL dynamics, responding to the increased balanced radial pressure gradient at the top of the TCBL, controls the ensuing enhancement of radial convergence (highlighted by the thick black arrows in

Fig. 15a) and the pattern of ascent out of the TCBL.[5] The thermodynamics of the TCBL, which was not evaluated here, also contributes to the development of diabatic heating, and thus is an essential element of boundary layer control. Within the TCBL, where the peak tangential wind is located, the symmetric radial advection of angular momentum maximizes just inside the RMW, contributing to spinup there, consistent with the composite tendency of the narrow TCs to intensify.

The question is then what aspect(s) of the broader TCs contribute to their tendency to weaken. We employ the same framework described above to elucidate key differences in the spinup mechanisms between broad and narrow TC composites. Figure 15b summarizes the structural characteristics observed for the broad vortex composite. While vertical motion at the top of the inflow layer within the eyewall was less than that observed for the narrow vortex (indicated by the shorter gray arrow within the eyewall in Fig. 15b), it is the difference between the lower- to middle-tropospheric convective mass flux and the mass flux at the top of the TCBL that best characterizes the ventilation (Smith et al. 2021). Again, although we did not directly measure the convective mass flux, the predominance of radial outflow above the TCBL and outside of the eyewall potentially highlights a reduced ability of eyewall convection to ventilate the air mass exiting the TCBL. The radial advective tendency for angular momentum was thus negative throughout most of the region between the top of the TCBL and 2.5-km altitude. This spindown tendency alone, through boundary layer control, would support a weakening of the peak tangential wind in the TCBL.

In contrast to the narrow vortex, however, the symmetric angular momentum tendency above the TCBL for the broad vortex was dominated by a positive contribution from vertical advection of angular momentum, particularly in the outer-core region. As noted earlier in the discussion above, and depicted in Fig. 15b, this significant difference in structure is likely related to a greater frequency of organized convection outside the eyewall. The development of secondary eyewall and rainband structures, which appear to be reflected here in the broad-vortex composite, is often related to pausing of intensification, or weakening (Rozoff et al. 2012; Didlake et al. 2017, 2018; Wang 2009; Molinari et al. 2019; Sitkowski et al. 2011). It may be that the intensification rate differences analyzed here are associated more with the presence or absence of secondary convective structures outside the eyewall than the particular radial vortex structure. In the TCBL of the broad vortex, both radial inflow and eyewall ascent within the inner-core region are noticeably smaller than in the narrow vortex, likely due to the "cutoff" effect of the secondary circulation associated with the outer rainband/eyewall features (Powell 1990; Barnes et al. 1983; Barnes and Powell 1995; Barnes 2008; Wroe and Barnes 2003). This "cutoff" effect hinders the secondary circulation of the (primary) eyewall.

Interestingly, Smith et al. (2021) also observed the development of rainbands which coincided with a broadening of the tangential wind profile in the outer-core region and a transient weakening period of the peak azimuthal-mean tangential wind in the TCBL. There they argued that outflow above the TCBL (associated with unventilated air within the eyewall) could have triggered/supported the development of the rainbands. In our composite study, it is difficult to establish such causation. Regardless of the mechanism for outer rainband or secondary eyewall formation, they also concluded that increased azimuthal coverage by outer-core organized convection was detrimental to the organization of eyewall convection and the net convective mass flux in the eyewall region. For the broad vortex composite, both the effect of reduced ventilation of the eyewall region and the "cutoff" effect associated with outer convection were apparently sufficient to reduce the radial inflow outside the RMW in the TCBL relative to the narrow vortex (indicated by the shorter thick black arrows in Fig. 15b). Consequently, the spinup tendency through the radial advection of angular momentum was limited, consistent with the composite tendency of the broad TCs to weaken. Further investigation of the various mechanisms described above (e.g., pertaining to the convective mass flux and the TCBL thermodynamics) is reserved for a future study combining profile, swath and dropsonde data.

It should be emphasized that one limitation of the analyses performed here is that they were conducted in an azimuthally averaged framework. This was done primarily because of the challenge in accurately estimating the eddy contributions to the flow using the profile analysis dataset. When a pronounced asymmetric structure of the TC is forced externally by the environmental flow or horizontal gradients of moisture or sea surface conditions, the early-stage intensification process in terms of the transition from an asymmetric to symmetric structure becomes important (e.g., Persing and Montgomery (2003); Guimond et al. 2016b; Montgomery and Smith 2017; Rios-Berrios et al. 2018). Rogers et al. (2016), using Doppler swath analyses of Hurricane Edouard (2014), noted that the lower-tropospheric inflow was stronger just outside the RMW, and extended further inside the RMW, in the downshear-right quadrant during the mission when Edouard was intensifying, compared to when Edouard was steady state. Both downdraft ventilation and midlevel (radial) ventilation constrain the TC development in shear (Riemer et al. 2010; Tang and Emanuel 2010, 2012; Molinari et al. 2013). Previous studies identified differences in surface enthalpy fluxes and thermodynamic recovery of downdraft-cooled air left of shear and on the upshear side as being an important distinguishing feature of intensifying (INT) versus steady-state (SS) TCs (Zhang et al. 2017a; Wadler et al. 2018, 2021; Nguyen at el. 2019; Chen et al. 2021; Finocchio and Rios-Berrios 2021; Alland et al. 2021; Alland and Davis 2022). Future work will thus involve expanding the analysis to include asymmetric processes in TC intensity change. This will involve using a combination of the TDR profile data with three-dimensional (swath) radar analyses that represent convection, IWRAP data that represent smaller eddy

---

[5] Kilroy et al. (2016) clarify that beneath and in the immediate vicinity of the eyewall updraft, the TCBL dynamics is not solely responsible for the radial and vertical flow structure. For example, the "suction effect" of convection also contributes to the flow evolution there.

scales, and dropsonde data that measures thermodynamic structure.

In addition to the fundamental insights into TCBL structure and TC intensity change gained from these composite analyses, our results have applications for improving numerical models. The observed structural differences between the broad (steady-state/weakening) and narrow (intensifying) vortices in this study argue for observations and data assimilation techniques that ensure that the radial structure of the vortex wind field is accurately captured in the initial conditions of forecast models. They also point to tests that can be performed in idealized simulations that can further evaluate the role of vortex structure in TCBL kinematic structure and intensity change. These structural differences can also be used for model physics evaluation purposes in terms of accurately prescribing physical parameterizations to reproduce the best possible wind radii, peak inflow location, PBL height, and updraft distribution, since the vortex shape is related to TC intensification rate as well. In the end, our analyses provide observational evidence for theoretical studies relating BL structure and TC intensity change processes and thus have the potential to improve forecasts of TC intensity.

REFERENCES

Ahern, K., M. A. Bourassa, R. E. Hart, J. A. Zhang, and R. F. Rogers, 2019: Observed kinematic and thermodynamic structure in the hurricane boundary layer during intensity change. *Mon. Wea. Rev.*, **147**, 2765–2785, https://doi.org/10.1175/MWR-D-18-0380.1.

Alland, J. J., and C. A. Davis, 2022: Effects of surface fluxes on ventilation pathways and the intensification of Hurricane Michael (2018). *J. Atmos. Sci.*, **79**, 1211–1229, https://doi.org/10.1175/JAS-D-21-0166.1.

——, B. H. Tang, K. L. Corbosiero, and G. H. Bryan, 2021: Combined effects of midlevel dry air and vertical wind shear on tropical cyclone development. Part I: Downdraft ventilation. *J. Atmos. Sci.*, **78**, 763–782, https://doi.org/10.1175/JAS-D-20-0054.1.

Atlas, D., R. C. Srivastava, and R. S. Sekhon, 1973: Doppler radar characteristics of precipitation at vertical incidence. *Rev. Geophys.*, **11**, 1–35, https://doi.org/10.1029/RG011i001p00001.

Barnes, G. M., 2008: Atypical thermodynamic profiles in hurricanes. *Mon. Wea. Rev.*, **136**, 631–643, https://doi.org/10.1175/2007MWR2033.1.

——, and M. D. Powell, 1995: Evolution of the inflow boundary layer of Hurricane Gilbert (1988). *Mon. Wea. Rev.*, **123**, 2348–2368, https://doi.org/10.1175/1520-0493(1995)123<2348:EOTIBL>2.0.CO;2.

——, E. J. Zipser, D. Jorgensen, and F. D. Marks Jr., 1983: Mesoscale and convective structure of a hurricane rainband. *J. Atmos. Sci.*, **40**, 2125–2137, https://doi.org/10.1175/1520-0469(1983)040<2125:MACSOA>2.0.CO;2.

Bell, M. M., and M. T. Montgomery, 2008: Observed structure, evolution, and potential intensity of category 5 Hurricane Isabel (2003) from 12 to 14 September. *Mon. Wea. Rev.*, **136**, 2023–2046, https://doi.org/10.1175/2007MWR1858.1.

Bryan, G. H., and R. Rotunno, 2009: The maximum intensity of tropical cyclones in axisymmetric numerical model simulations. *Mon. Wea. Rev.*, **137**, 1770–1789, https://doi.org/10.1175/2008MWR2709.1.

Cangialosi, J. P., E. Blake, M. DeMaria, A. Penny, A. Latto, E. Rappaport, and V. Tallapragada, 2020: Recent progress in tropical cyclone intensity forecasting at the National Hurricane Center. *Wea. Forecasting*, **35**, 1913–1922, https://doi.org/10.1175/WAF-D-20-0059.1.

Chen, X., J.-F. Gu, J. A. Zhang, F. D. Marks, R. F. Rogers, and J. J. Cione, 2021: Boundary layer recovery and precipitation symmetrization preceding rapid intensification of tropical cyclones under shear. *J. Atmos. Sci.*, **78**, 1523–1544, https://doi.org/10.1175/JAS-D-20-0252.1.

Didlake, A. C., Jr., G. H. Heymsfield, P. D. Reasor, and S. R. Guimond, 2017: Concentric eyewall asymmetries in Gonzalo (2014) observed by airborne radar. *Mon. Wea. Rev.*, **145**, 729–749, https://doi.org/10.1175/MWR-D-16-0175.1.

——, P. D. Reasor, R. F. Rogers, and W.-C. Lee, 2018: Dynamics of the transition from spiral rainbands to a secondary eyewall in Hurricane Earl (2010). *J. Atmos. Sci.*, **75**, 2909–2929, https://doi.org/10.1175/JAS-D-17-0348.1.

Emanuel, K. A., 1986: An air–sea interaction theory for tropical cyclones. Part I: Steady-state maintenance. *J. Atmos. Sci.*, **43**, 585–605, https://doi.org/10.1175/1520-0469(1986)043<0585:AASITF>2.0.CO;2.

——, 1995: Sensitivity of tropical cyclones to surface exchange coefficients and a revised steady-state model incorporating eye dynamics. *J. Atmos. Sci.*, **52**, 3969–3976, https://doi.org/10.1175/1520-0469(1995)052<3969:SOTCTS>2.0.CO;2.

Finocchio, P. M., and R. Rios-Berrios, 2021: The intensity- and size-dependent response of tropical cyclones to increasing vertical wind shear. *J. Atmos. Sci.*, **78**, 3673–3690, https://doi.org/10.1175/JAS-D-21-0126.1.

Fischer, M. S., P. D. Reasor, R. F. Rogers, and J. F. Gamache, 2022: An analysis of tropical cyclone vortex and convective

characteristics in relation to storm intensity using a novel airborne Doppler radar database. *Mon. Wea. Rev.*, **150**, 2255–2278, https://doi.org/10.1175/MWR-D-21-0223.1.

Gall, R., J. Franklin, F. Marks, E. N. Rappaport, and F. Toepfer, 2013: The Hurricane Forecast Improvement Project. *Bull. Amer. Meteor. Soc.*, **94**, 329–343, https://doi.org/10.1175/BAMS-D-12-00071.1.

Gamache, J. F., F. D. Marks Jr., and F. Roux, 1995: Comparison of three airborne Doppler sampling techniques with airborne in situ wind observations in Hurricane Gustav (1990). *J. Atmos. Oceanic Technol.*, **12**, 171–181, https://doi.org/10.1175/1520-0426(1995)012<0171:COTADS>2.0.CO;2.

Guimond, S. R., G. M. Heymsfield, P. D. Reasor, and A. C. Didlake Jr., 2016a: The rapid intensification of Hurricane Karl (2010): New remote sensing observations of convective bursts from the Global Hawk platform. *J. Atmos. Sci.*, **73**, 3617–3639, https://doi.org/10.1175/JAS-D-16-0026.1.

——, J. M. Reisner, S. Marras, and F. X. Giraldo, 2016b: The impacts of dry dynamic cores on asymmetric hurricane intensification. *J. Atmos. Sci.*, **73**, 4661–4684, https://doi.org/10.1175/JAS-D-16-0055.1.

——, J. A. Zhang, J. W. Sapp, and S. J. Frasier, 2018: Coherent turbulence in the boundary layer of Hurricane Rita (2005) during an eyewall replacement cycle. *J. Atmos. Sci.*, **75**, 3071–3093, https://doi.org/10.1175/JAS-D-17-0347.1.

——, P. Reasor, G. M. Heymsfield, and M. M. McLinden, 2020: The dynamics of vortex Rossby waves and secondary eyewall development in Hurricane Matthew (2016): New insights from radar measurements. *J. Atmos. Sci.*, **77**, 2349–2374, https://doi.org/10.1175/JAS-D-19-0284.1.

Hack, J. J., and W. H. Schubert, 1986: Nonlinear response of atmospheric vortices to heating by organized cumulus convection. *J. Atmos. Sci.*, **43**, 1559–1573, https://doi.org/10.1175/1520-0469(1986)043<1559:NROAVT>2.0.CO;2.

Heng, J., and Y. Wang, 2016: Nonlinear response of a tropical cyclone vortex to prescribed eyewall heating with and without surface friction in TCM4: Implications for tropical cyclone intensification. *J. Atmos. Sci.*, **73**, 1315–1333, https://doi.org/10.1175/JAS-D-15-0164.1.

Huang, Y.-H., M. T. Montgomery, and C.-C. Wu, 2012: Concentric eyewall formation in Typhoon Sinlaku (2008). Part II: Axisymmetric dynamical processes. *J. Atmos. Sci.*, **69**, 662–674, https://doi.org/10.1175/JAS-D-11-0114.1.

Joss, J., and A. Waldvogel, 1970: Raindrop size distribution and Doppler velocities. Preprints, *14th Radar Meteor. Conf.*, Tucson, AZ, Amer. Meteor. Soc., 153–156.

Kaplan, J., and Coauthors, 2015: Evaluating environmental impacts on tropical cyclone rapid intensification predictability utilizing statistical models. *Wea. Forecasting*, **30**, 1374–1396, https://doi.org/10.1175/WAF-D-15-0032.1.

Kepert, J. D., 2001: The dynamics of boundary layer jets within the tropical cyclone core. Part II: Nonlinear enhancement. *J. Atmos. Sci.*, **58**, 2485–2501, https://doi.org/10.1175/1520-0469(2001)058<2485:TDOBLJ>2.0.CO;2.

——, 2013: How does the boundary layer contribute to eyewall replacement cycles in axisymmetric tropical cyclones? *J. Atmos. Sci.*, **70**, 2808–2830, https://doi.org/10.1175/JAS-D-13-046.1.

——, 2017: Time and space scales in the tropical cyclone boundary layer, and the location of the eyewall updraft. *J. Atmos. Sci.*, **74**, 3305–3323, https://doi.org/10.1175/JAS-D-17-0077.1.

——, and D. S. Nolan, 2014: Reply to "Comments on 'How does the boundary layer contribute to eyewall replacement cycles in

axisymmetric tropical cyclones?'" *J. Atmos. Sci.*, **71**, 4692–4704, https://doi.org/10.1175/JAS-D-14-0014.1.

Kilroy, G., R. K. Smith, and M. T. Montgomery, 2016: Why do model tropical cyclones grow progressively in size and decay in intensity after reaching maturity? *J. Atmos. Sci.*, **73**, 487–503, https://doi.org/10.1175/JAS-D-15-0157.1.

——, ——, and ——, 2017a: A unified view of tropical cyclogenesis and intensification. *Quart. J. Roy. Meteor. Soc.*, **143**, 450–462, https://doi.org/10.1002/qj.2934.

——, M. T. Montgomery, and R. K. Smith, 2017b: The role of boundary-layer friction on tropical cyclogenesis and subsequent intensification. *Quart. J. Roy. Meteor. Soc.*, **143**, 2524–2536, https://doi.org/10.1002/qj.3104.

Lee, W.-C., P. Dodge, F. D. Marks Jr., and P. H. Hildebrand, 1994: Mapping of airborne Doppler radar data. *J. Atmos. Oceanic Technol.*, **11**, 572–578, https://doi.org/10.1175/1520-0426(1994)011<0572:MOADRD>2.0.CO;2.

Leighton, H., S. Gopalakrishnan, J. A. Zhang, R. F. Rogers, Z. Zhang, and V. Tallapragada, 2018: Azimuthal distribution of deep convection, environmental factors, and tropical cyclone rapid intensification: A perspective from HWRF ensemble forecasts of Hurricane Edouard (2014). *J. Atmos. Sci.*, **75**, 275–295, https://doi.org/10.1175/JAS-D-17-0171.1.

Lorsolo, S., J. A. Zhang, F. Marks Jr., and J. Gamache, 2010: Estimation and mapping of hurricane turbulent energy using airborne Doppler measurements. *Mon. Wea. Rev.*, **138**, 3656–3670, https://doi.org/10.1175/2010MWR3183.1.

Marks, F. D., Jr., 1985: Evolution of the structure of precipitation in Hurricane Allen (1980). *Mon. Wea. Rev.*, **113**, 909–930, https://doi.org/10.1175/1520-0493(1985)113<0909:EOTSOP>2.0.CO;2.

——, and R. A. Houze Jr., 1987: Inner core structure of Hurricane Alicia from airborne Doppler radar observations. *J. Atmos. Sci.*, **44**, 1296–1317, https://doi.org/10.1175/1520-0469(1987)044<1296:ICSOHA>2.0.CO;2.

——, ——, and J. F. Gamache, 1992: Dual-aircraft investigation of the inner core of Hurricane Norbert. Part I: Kinematic structure. *J. Atmos. Sci.*, **49**, 919–942, https://doi.org/10.1175/1520-0469(1992)049<0919:DAIOTI>2.0.CO;2.

——, P. G. Black, M. T. Montgomery, and R. W. Burpee, 2008: Structure of the eye and eyewall of Hurricane Hugo (1989). *Mon. Wea. Rev.*, **136**, 1237–1259, https://doi.org/10.1175/2007MWR2073.1.

Ming, J., J. A. Zhang, and R. F. Rogers, 2015: Typhoon kinematic and thermodynamic boundary layer structure from dropsonde composites. *J. Geophys. Res. Atmos.*, **120**, 3158–3172, https://doi.org/10.1002/2014JD022640.

Molinari, J., J. Frank, and D. Vollaro, 2013: Convective bursts, downdraft cooling, and boundary layer recovery in a sheared tropical storm. *Mon. Wea. Rev.*, **141**, 1048–1060, https://doi.org/10.1175/MWR-D-12-00135.1.

——, J. A. Zhang, R. F. Rogers, and D. Vollaro, 2019: Repeated eyewall replacement cycles in Hurricane Frances (2004). *Mon. Wea. Rev.*, **147**, 2009–2022, https://doi.org/10.1175/MWR-D-18-0345.1.

Montgomery, M. T., and R. K. Smith, 2014: Paradigms for tropical cyclone intensification. *Aust. Meteor. Oceanogr. J.*, **64**, 37–66, https://doi.org/10.22499/2.6401.005.

——, and ——, 2017: Recent developments in the fluid dynamics of tropical cyclones. *Annu. Rev. Fluid Mech.*, **49**, 541–574, https://doi.org/10.1146/annurev-fluid-010816-060022.

——, J. A. Zhang, and R. K. Smith, 2014a: An analysis of the observed low-level structure of rapidly intensifying and mature

Hurricane Earl (2010). *Quart. J. Roy. Meteor. Soc.*, **140**, 2132–2146, https://doi.org/10.1002/qj.2283.

——, S. F. Abarca, R. K. Smith, C.-C. Wu, and Y.-H. Huang, 2014b: Comments on "How does the boundary layer contribute to eyewall replacement cycles in axisymmetric tropical cyclones?" *J. Atmos. Sci.*, **71**, 4682–4691, https://doi.org/10.1175/JAS-D-13-0286.1.

Nguyen, L. T., R. Rogers, J. Zawislak, and J. A. Zhang, 2019: Assessing the influence of convective downdrafts and surface enthalpy fluxes on tropical cyclone intensity change in moderate vertical wind shear. *Mon. Wea. Rev.*, **147**, 3519–3534, https://doi.org/10.1175/MWR-D-18-0461.1.

Nolan, D. S., Y. Moon, and D. P. Stern, 2007: Tropical cyclone intensification from asymmetric convection: Energetics and efficiency. *J. Atmos. Sci.*, **64**, 3377–3405, https://doi.org/10.1175/JAS3988.1.

Ooyama, K., 1969: Numerical simulation of the life cycle of tropical cyclones. *J. Atmos. Sci.*, **26**, 3–40, https://doi.org/10.1175/1520-0469(1969)026<0003:NSOTLC>2.0.CO;2.

Pendergrass, A. G., and H. E. Willoughby, 2009: Diabatically induced secondary flows in tropical cyclones. Part I: Quasi-steady forcing. *Mon. Wea. Rev.*, **137**, 805–821, https://doi.org/10.1175/2008MWR2657.1.

Persing, J., and M. T. Montgomery, 2003: Hurricane superintensity. *J. Atmos. Sci.*, **60**, 2349–2371, https://doi.org/10.1175/1520-0469(2003)060<2349:HS>2.0.CO;2.

——, ——, J. C. McWilliams, and R. K. Smith, 2013: Asymmetric and axisymmetric dynamics of tropical cyclones. *Atmos. Chem. Phys.*, **13**, 12 299–12 341, https://doi.org/10.5194/acp-13-12299-2013.

Powell, M. D., 1990: Boundary layer structure and dynamics in outer hurricane rainbands. Part II: Downdraft modification and mixed layer recovery. *Mon. Wea. Rev.*, **118**, 918–938, https://doi.org/10.1175/1520-0493(1990)118<0918:BLSADI>2.0.CO;2.

Reasor, P. D., and M. D. Eastin, 2012: Rapidly intensifying Hurricane Guillermo (1997). Part II: Resilience in shear. *Mon. Wea. Rev.*, **140**, 425–444, https://doi.org/10.1175/MWR-D-11-00080.1.

Riemer, M., M. T. Montgomery, and M. E. Nicholls, 2010: A new paradigm for intensity modification of tropical cyclones: Thermodynamic impact of vertical wind shear on the inflow layer. *Atmos. Chem. Phys.*, **10**, 3163–3188, https://doi.org/10.5194/acp-10-3163-2010.

Rios-Berrios, R., C. A. Davis, and R. D. Torn, 2018: A hypothesis for the intensification of tropical cyclones under moderate vertical wind shear. *J. Atmos. Sci.*, **75**, 4149–4173, https://doi.org/10.1175/JAS-D-18-0070.1.

Rogers, R. F., S. Lorsolo, P. Reasor, J. Gamache, and F. D. Marks Jr., 2012: Multiscale analysis of tropical cyclone kinematic structure from airborne Doppler radar composites. *Mon. Wea. Rev.*, **140**, 77–99, https://doi.org/10.1175/MWR-D-10-05075.1.

——, P. D. Reasor, and S. Lorsolo, 2013: Airborne Doppler observations of the inner-core structural differences between intensifying and steady-state tropical cyclones. *Mon. Wea. Rev.*, **141**, 2970–2991, https://doi.org/10.1175/MWR-D-12-00357.1.

——, ——, and J. A. Zhang, 2015: Multiscale structure and evolution of Hurricane Earl (2010) during rapid intensification. *Mon. Wea. Rev.*, **143**, 536–562, https://doi.org/10.1175/MWR-D-14-00175.1.

——, J. A. Zhang, J. Zawislak, H. Jiang, G. R. Alvey III, E. J. Zipser, and S. N. Stevenson, 2016: Observations of the structure and evolution of Hurricane Edouard (2014) during intensity change. Part II: Kinematic structure and the distribution of deep convection. *Mon. Wea. Rev.*, **144**, 3355–3376, https://doi.org/10.1175/MWR-D-16-0017.1.

——, C. S. Velden, J. A. Zawislak, and J. A. Zhang, 2019: Tropical cyclones and hurricanes: Observations. *Reference Module in Earth Systems and Environmental Sciences*, Elsevier, 25, https://doi.org/10.1016/B978-0-12-409548-9.12065-2.

Rozoff, C. M., W. H. Schubert, and J. P. Kossin, 2008: Some dynamical aspects of tropical cyclone concentric eyewalls. *Quart. J. Roy. Meteor. Soc.*, **134**, 583–593, https://doi.org/10.1002/qj.237.

——, D. S. Nolan, J. P. Kossin, F. Zhang, and J. Fang, 2012: The roles of an expanding wind field and inertial stability in tropical cyclone secondary eyewall formation. *J. Atmos. Sci.*, **69**, 2621–2643, https://doi.org/10.1175/JAS-D-11-0326.1.

Sanger, N. T., M. T. Montgomery, R. K. Smith, and M. M. Bell, 2014: An observational study of tropical cyclone spinup in Supertyphoon Jangmi (2008) from 24 to 27 September. *Mon. Wea. Rev.*, **142**, 3–28, https://doi.org/10.1175/MWR-D-12-00306.1.

Schubert, W. H., and J. J. Hack, 1982: Inertial stability and tropical cyclone development. *J. Atmos. Sci.*, **39**, 1687–1697, https://doi.org/10.1175/1520-0469(1982)039<1687:ISATCD>2.0.CO;2.

Shapiro, L. J., and H. E. Willoughby, 1982: The response of balanced hurricanes to local sources of heat and momentum. *J. Atmos. Sci.*, **39**, 378–394, https://doi.org/10.1175/1520-0469(1982)039<0378:TROBHT>2.0.CO;2.

Sitkowski, M., J. P. Kossin, and C. M. Rozoff, 2011: Intensity and structure changes during hurricane eyewall replacement cycles. *Mon. Wea. Rev.*, **139**, 3829–3847, https://doi.org/10.1175/MWR-D-11-00034.1.

Smith, R. K., and M. T. Montgomery, 2016: The efficiency of diabatic heating and tropical cyclone intensification. *Quart. J. Roy. Meteor. Soc.*, **142**, 2081–2086, https://doi.org/10.1002/qj.2804.

——, and ——, 2020: The generalized Ekman model for the tropical cyclone boundary layer revisited: The myth of inertial stability as a restoring force. *Quart. J. Roy. Meteor. Soc.*, **146**, 3435–3449, https://doi.org/10.1002/qj.3854.

——, ——, and N. Van Sang, 2009: Tropical cyclone spin-up revisited. *Quart. J. Roy. Meteor. Soc.*, **135**, 1321–1335, https://doi.org/10.1002/qj.428.

——, J. A. Zhang, and M. T. Montgomery, 2017: The dynamics of intensification in a hurricane weather research and forecasting simulation of Hurricane Earl (2010). *Quart. J. Roy. Meteor. Soc.*, **143**, 293–308, https://doi.org/10.1002/qj.2922.

——, G. Kilroy, and M. T. Montgomery, 2021: Tropical cyclone life cycle in a three-dimensional numerical simulation. *Quart. J. Roy. Meteor. Soc.*, **147**, 3373–3393, https://doi.org/10.1002/qj.4133.

Sroka, S., and S. R. Guimond, 2021: Organized kinetic energy backscatter in the hurricane boundary layer from radar measurements. *J. Fluid Mech.*, **924**, A21, https://doi.org/10.1017/jfm.2021.632.

Stevenson, S. N., K. L. Corbosiero, M. DeMaria, and J. L. Vigh, 2018: A 10-year survey of tropical cyclone inner-core lightning bursts and their relationship to intensity change. *Wea. Forecasting*, **33**, 23–36, https://doi.org/10.1175/WAF-D-17-0096.1.

Tang, B., and K. Emanuel, 2010: Midlevel ventilation's constraint on tropical cyclone intensity. *J. Atmos. Sci.*, **67**, 1817–1830, https://doi.org/10.1175/2010JAS3318.1.

——, and ——, 2012: Sensitivity of tropical cyclone intensity to ventilation in an axisymmetric model. *J. Atmos. Sci.*, **69**, 2394–2413, https://doi.org/10.1175/JAS-D-11-0232.1.

Vigh, J. L., and W. H. Schubert, 2009: Rapid development of the tropical cyclone warm core. *J. Atmos. Sci.*, **66**, 3335–3350, https://doi.org/10.1175/2009JAS3092.1.

Wadler, J. B., J. A. Zhang, B. Jaimes, and L. K. Shay, 2018: Downdrafts and the evolution of boundary layer thermodynamics in Hurricane Earl (2010) before and during rapid intensification. *Mon. Wea. Rev.*, **146**, 3545–3565, https://doi.org/10.1175/MWR-D-18-0090.1.

——, ——, R. F. Rogers, B. Jaimes, and L. K. Shay, 2021: The rapid intensification of Hurricane Michael (2018): Storm structure and the relationship to environmental and air–sea interactions. *Mon. Wea. Rev.*, **149**, 245–267, https://doi.org/10.1175/MWR-D-20-0145.1.

Wang, Y., 2009: How do outer spiral rainbands affect tropical cyclone structure and intensity? *J. Atmos. Sci.*, **66**, 1250–1273, https://doi.org/10.1175/2008JAS2737.1.

Wroe, D. R., and G. M. Barnes, 2003: Inflow layer energetics of Hurricane Bonnie (1998) near landfall. *Mon. Wea. Rev.*, **131**, 1600–1612, https://doi.org/10.1175//2547.1.

Zhang, J. A., and F. D. Marks, 2015: Effects of horizontal eddy diffusion on tropical cyclone intensity change and structure in idealized three-dimensional numerical simulations. *Mon.*

Wea. Rev., **143**, 3981–3995, https://doi.org/10.1175/MWR-D-14-00341.1.

——, and R. F. Rogers, 2019: Effects of parameterized boundary layer structure on hurricane rapid intensification in shear. *Mon. Wea. Rev.*, **147**, 853–871, https://doi.org/10.1175/MWR-D-18-0010.1.

——, ——, D. S. Nolan, and F. D. Marks Jr., 2011: On the characteristic height scales of the hurricane boundary layer. *Mon. Wea. Rev.*, **139**, 2523–2535, https://doi.org/10.1175/MWR-D-10-05017.1.

——, D. S. Nolan, R. F. Rogers, and V. Tallapragada, 2015: Evaluating the impact of improvements in the boundary layer parameterization on hurricane intensity and structure forecasts in HWRF. *Mon. Wea. Rev.*, **143**, 3136–3155, https://doi.org/10.1175/MWR-D-14-00339.1.

——, J. J. Cione, E. A. Kalina, E. W. Uhlhorn, T. Hock, and J. A. Smith, 2017a: Observations of infrared sea surface temperature and air-sea interaction in Hurricane Edouard (2014). *J. Atmos. Oceanic Technol.*, **34**, 1333–1349, https://doi.org/10.1175/JTECH-D-16-0211.1.

——, R. F. Rogers, and V. Tallapragada, 2017b: Impact of parameterized boundary layer structure on tropical cyclone rapid intensification forecasts in HWRF. *Mon. Wea. Rev.*, **145**, 1413–1426, https://doi.org/10.1175/MWR-D-16-0129.1.